High-altitude atmospheric turbulence and infrasound measurements using a balloon-launched small uncrewed aircraft system

Anisa N. Haghighi[1], Ryan D. Nolin[1], Gary D. Pundsack[2], Nick Craine[2], Aliaksei Stratsilatau[3], and Sean C. C. Bailey[1]

[1]Department of Mechanical and Aerospace Engineering, University of Kentucky, Lexington, Kentucky 40506, USA
[2]Stratodynamics Inc., 16192 Coastal Highway, Lewes, Delaware 19958, USA
[3]UAVOS Inc., 541 Jefferson Ave, Ste 100, Redwood City, California 94063, USA

Correspondence: Sean Bailey (sean.bailey@uky.edu)

Abstract. This study investigates the use of a balloon-launched small Uncrewed Aircraft System (sUAS) for the measurement of turbulence in the troposphere and lower stratosphere. The sUAS was a glider which could conduct an automated descent following a designated flight trajectory and equipped with in-situ sensors for measuring thermodyanamic and kinematic atmospheric properties typically measured using balloon-borne instruments. The trajectory of the glider allowed for improved statistical convergence and higher spatial resolution of derived statistics measured by the in-situ sensors. In addition, this aircraft was equipped with an infrasonic microphone to assess its suitability for the remote detection of clear-air turbulence. The capabilities of the sUAS and sensing systems were tested using three flights conducted in 2021 in New Mexico. It was found that the profiles of temperature, humidity and horizontal winds measured during descent were consistent with those made by radiosonde. Importantly, analysis of the statistics produced along the flight trajectory allowed the identification of key turbulence quantities and features such as gravity waves, thermals and tropopause folding, which allowed the connection to be made between the locations of increased turbulence intensity and the source of its generation. In addition, the infrasonic microphone amplitude was found to be correlated with the measurements of turbulence intensity, indicating that the microphone was sensing turbulence. However, interpretation of the microphone signal was convoluted by the altitude dependence of the microphone response and the difficulty in discriminating individual sources from within the microphone signal.

1 Introduction

Due to its importance in weather and climate, the formation and evolution of atmospheric turbulence has long been of scientific interest. In addition, the presence of atmospheric turbulence also poses an aviation hazard that is challenging to predict and detect. This latter point is particularly true for high-altitude autonomous flight, a regime which is being increasingly pursued in the form of High-Altitude Pseudo-Satellite, or High-Altitude Platform Station, (HAPS) aircraft, which can provide

communication and remote observation capabilities at relatively low cost. By the nature of the flight conditions under which these aircraft operate, they tend to be structurally fragile with narrow performance envelopes for which controlled flight can be maintained.

25 Despite the thermal inversion in the stratosphere indicating the presence of static stability, turbulence can still occur in this cloudless atmospheric layer due to mechanical or thermal disturbances, and thus often referred to as clear air turbulence. There are several potential sources of clear air turbulence. For example, the horizontal movement of air above terrain (e.g. mountains) can result in upward vertical motions, wind shear and turbulence production within their proximity. These motions are usually in the form of mountain waves (or lee waves) produced over the mountains by wind shear and their strength is determined by the height of the mountain and the strength of the wind. Another source of clear air turbulence is the presence of a jet stream. Jet

30 streams generally occur at the tropopause (the boundary region between the troposphere and stratosphere) and are a product of temperature gradients within the surrounding air. These sources of clear air turbulence can all pose hazards to small Uncrewed Aircraft Systems (sUAS)s and better measurement of these turbulence-generating mechanisms can potentially lead to better prediction and mitigation of the hazards they pose.

Many experiments have conducted stratospheric turbulence measurement using balloon-borne instruments (e.g. Wescott

35 et al., 1964; Ehrenberger, 1992; Haack et al., 2014) with previously published studies of stratospheric turbulence dating back to the 1960s (Enlich and Mancuso, 1968). Among the most relevant conclusions from these studies is that stratospheric turbulence tends to form in relatively thin atmospheric layers due to intrinsic static stability at these altitudes. Previous studies have also compared instances of high turbulent kinetic energy dissipation rate, ε, to the local Richardson number, Ri, to estimate if the turbulence arose from a convective or mechanical source of turbulence (Söder et al., 2021; Sharman et al., 2014; Kim et al.,

40 2020), with these results used to model the relationship between turbulence in the stratosphere as well as tropospheric activity (Chunchuzov et al., 2021).

One series of experiments focused on stratospheric turbulence has been the Leibniz-Institute Turbulence Observations in the Stratosphere (LITOS) experiments. These experiments consisted of balloons equipped with a thermal anemometer specifically intended to measure velocity and temperature fluctuations at high frequency. The resulting measurements were within sub-

45 centimeter resolution, and therefore suitable for resolving the finer scales of turbulence. This experiment reached altitudes up to 30 km, and ε was compared to both Ri and the square Brunt-Väisälä frequency, N^2 as a function of altitude. There was a noted increase in ε with altitude and clear correlation between turbulent events and $Ri < 0.25$. However, in some instances turbulent events were also observed where $Ri > 0.25$ although other studies attribute such behavior to the specifics of the Ri calculation, casting question as to its value as an indicator for the likelihood of turbulence development (Galperin et al., 2007;

50 Haack et al., 2014). LITOS experiments also investigated the phenomonon of tropopause folding, in which a stratospheric intrusion of air sinks below the upper tropospheric jet stream. The observational result was that dissipation rates above the upper-tropospheric jet were three orders of magnitude larger than below it (Söder et al., 2021) with deeper tropopause folds producing more severe turbulence.

Routine crewed aircraft measurements of atmospheric turbulence are also conducted, for example through the use of an

55 in-situ turbulence detection algorithm developed by the National Center for Atmospheric Research (NCAR) and implemented

on some 200 aircraft (Sharman et al., 2014) and through Aircraft Meteorological Data Relay (AMDAR) reports generated by in-situ measurement systems on commercial aircraft. These systems generally report the the turbulence intensity using the metric of eddy dissipation rate (EDR), defined as

$$EDR = \varepsilon^{1/3}, \tag{1}$$

which is currently used as a standard for turbulence reporting by the International Civil Aviation Organization (ICAO). In the NCAR EDR calculation, a fully-formed von Kármán inertial subrange is assumed, and the EDR is determined from with either vertical-wind measurements, or the aircraft's gust response measured through acceleration.

Recently, it has become increasingly common to use sUAS equipped with in-situ sensors (e.g. hot-wire anemometers, sonic anemometers, hot-film probes, multi-hole pressure probes) for studies of turbulence in the atmospheric boundary layer and troposphere (e.g. Egger et al., 2002; Hobbs et al., 2002; Balsley et al., 2013; Witte et al., 2017; Rautenberg et al., 2018; Bärfuss et al., 2018; Jacob et al., 2018; Bailey et al., 2019; Al-Ghussain and Bailey, 2022). Many of the sUAS used for turbulence studies employ multi-hole probes, which measure the dynamic pressure of the air, with multiple pressure ports combined with a directional calibration to determine the wind vector relative to the probe axis. Due to their fragility, hot-wire probes, which measure the convective heat transfer across a very thin heated filament, are usually reserved for short-term scientific studies although they are standard instruments on some sUAS (Hamilton et al., 2022). The fast response of the hot-wire anemometer allows detailed characterization of the turbulence, for example allowing the measurement of small-scale fluctuations corresponding to turbulent dissipation.

An additional sensing system which has potential to measure clear air turbulence are infrasonic microphones (Cuxart et al., 2015; Shams et al., 2013). These infrasound sensors are capable of detecting acoustic frequencies below 20 Hz and are typically used for seismic detection and marine acoustics. Within the atmospheric boundary layer, the infrasound energy from ground-based arrays has been found to correspond to the turbulent kinetic energy in the atmosphere, particularly when buoyantly-produced convective turbulence is present. The infrasound energy levels also seem to be higher when there were elevated jets or turbulence above the measurement height, which was thought to be caused by the sound generated at higher altitudes reaching the microphones. In balloon-borne measurements, it has been found that it is possible to detect acoustic low frequency signals, such as microbaroms, using sensitive infrasonic sensors (Bowman and Lees, 2015). The advantage of infrasonic sensors for turbulence detection is that acoustic propagation increases at low frequency and low kinematic viscosity (Whitaker and Norris, 2008) allows propagation over distances ranging between a few hundred to a few thousand of kilometers. For example, an array of ground-based microphones were able to detect clear air turbulence at distances up to 360 km (Shams et al., 2013).

Despite over a century of work in turbulence detection, predicting the production, presence and characteristics of turbulence in the atmosphere is still a significant challenge. Hence, in-situ observations are still invaluable both as a research tool and for routine observation. However, due to the transient nature of their Lagrangian flight trajectory, balloon-based approaches are not necessarily amenable to obtaining detailed statistical descriptions of turbulence at high altitudes. Here, we examine the potential of using a balloon-launched stratospheric glider sUAS for turbulence measurement. A glider offers advantages

over traditional balloon launches by being able to maximize time at altitude during its descent phase, by being able to transect

90 moving and interacting air masses, and by maintaining a relatively geostationary position during its descent. These qualities facilitate the statistical analysis necessary for quantification of non-stationary properties. For these measurements, the aircraft was equipped both with traditional in-situ sensors as well as a novel infrasonic microphone in order to test the potential of using airborne acoustic signatures to remotely detect the presence of turbulence. This configuration was tested in a series of three high-altitude flight tests conducted at Spaceport America in New Mexico USA, conducting measurements from 25 km to

95 30 km above sea level down to the surface.

The remainder of this manuscript is divided into three main sections: Section 2 describes the aircraft and measurement systems, along with information about the flight location and flight path; Section 3 overviews the observations made, including profiles of key statistics and infrasonic microphone response as well as horizontal distributions of key quantities; with Section 4 summarizing the main findings from this study.

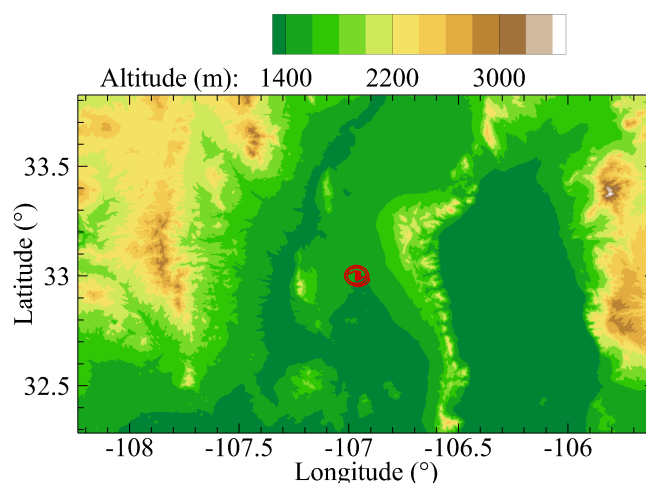## 2   Experiment Description

2.1   Overview

Figure 1. The topography of the flight area with Spaceport America with the trajectory of Flight 3 indicated by a red line to illustrate region of measurement.

The measurement campaign was conducted at Spaceport America, located near Truth or Consequences, New Mexico, U.S.A. between the Black Range and San Andres mountain ranges (Fig. 1), from June 1, 2021 through June 6, 2021. Three flights were flown, with Flight 1 being conducted on June 1; Flight 2 conducted on June 4; and Flight 3 being conducted on June 6. Each

105 flight consisted of a weather-balloon carrying the glider aloft to a release altitude of 25 km above sea level (m.s.l.) for Flights 1 and 2, and 30 km m.s.l. for Flight 3. After release, the aircraft conducted an automated descent along a pre-determined flight

path down to the Spaceport America runway. Details of the aircraft, payload, procedures and flight trajectories are provided below.
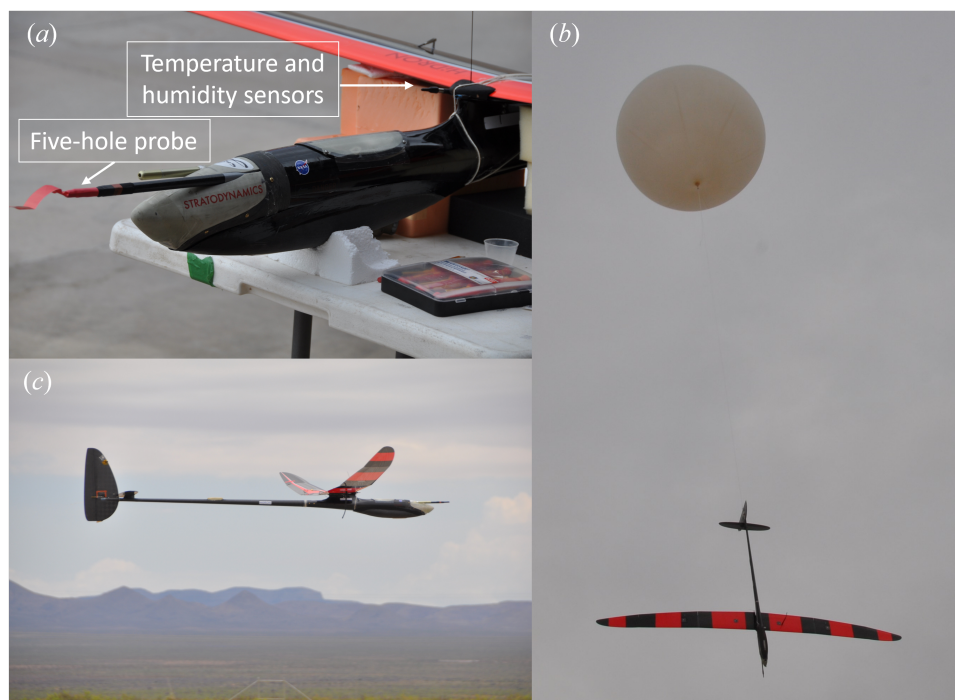

Figure 2. Images of HiDRON H2 showing: (*a*) close up of aircraft nose showing five-hole probe and temperature and humidity sensor location; (*b*) aircraft during launch; and (*c*) aircraft during landing.

2.2 Aircraft

110 Key to this research was the use of the host sUAS platform, the HiDRON H2 (see Fig. 2), operated by Stratodynamics Inc. The HiDRON H2 is a balloon-launched carbon fiber/fiberglass glider sUAS that is capable of autonomous and soaring flight modes. It has a wingspan of 3.8 m and its nominal flight weight is approximately 5.7 kg with the payload. To achieve initial altitudes in excess of 30 km, the HiDRON H2 is launched using latex sounding balloons. Different sizes of balloons were used with 2000 g, 1200 g and 3000 g employed for Flights 1, 2 and 3, respectively. After release, the aircraft is controlled by a UAVOS Inc.

115 autopilot to follow a pre-programmed descent pattern towards a designated landing point. An operator can track the HiDRON H2 position from launch to landing and changes to the flight plan can be made in real time through radio telemetry, which also allows operational parameters to be transmitted to the ground with a range of 100 km. Full telemetry information was produced at 10 Hz by the autopilot for all three flights, including location, ground speed, 6 degree-of-freedom orientation information and pressure, temperature and humidity information from the integrated iMet-XF atmospheric sensors. Other safety features

120 include a parachute, dual-redundant balloon release system and geofencing safety protocols that prevent the aircraft from leaving the designated airspace. During prior flights, including flights exceeding altitude of 30 km, the HiDRON H2 has shown

reliability in remaining controllable in high-wind (114 km h^{-1}) and low-temperature conditions ($< -60°$C) and in returning to a predefined landing site.

To measure atmospheric conditions, the aircraft was equipped with an integrated InterMet Systems iMet-XF system having fast-response bead thermistor air temperature and humidity sensors. The pressure sensor provided a ±1.5 hPa accuracy for pressure, with humidity sensor supporting a full 0 - 100 %RH range at $\pm$ 5 %RH accuracy with a resolution of 0.7 %RH. The temperature sensor provided a $\pm$ 0.3°C accuracy with a resolution of 0.01°C up to a maximum of 50°C. The stated response times of these sensors are on the order of 10 ms for pressure, 5 s for humidity and 2 s for temperature in still air, with the autopilot sampling these sensors at 10 Hz. The pressure and temperature sensors were mounted with the sensing elements exposed to the airflow upstream of the wing support (see Fig. 2a) to ensure sufficient aspiration of the sensors.

2.3 Payload

The turbulence-measuring payload was a combination of four components: (1) five-hole probe; (2) infrasonic sensor; (3) data acquisition board; and (4) embedded computer. These components were installed in the nose of the HiDRON H2, which could be accessed via removal of the nose cone, as shown in Fig. 3c.

Figure 3. (*a*) Five-hole probe prior to addition of heating element, (*b*) Infrasonic microphone, and (*c*) Nose payload bay open between flights, with embedded computer shown removed for data retrieval. Infrasonic microphone is below embedded computer but was installed in aircraft nose facing forward during flight.

2.3.1 Five-Hole Probe:

Wind speed and direction relative to the aircraft were measured using a bespoke five-hole probe mounted such that the probe projected upstream of the nose of the aircraft, as shown in Fig. 2. The probe, detailed in Fig. 3a, was a carbon-fiber tube equipped with a beveled aluminum tip. The tip of the probe was arranged with one center hole normal to the probe axis surrounded by four other holes arranged symmetrically around the center hole with their plane normal vector aligned 20° to the probe axis. For this measurement, the pressure difference between central hole (measuring total stagnation pressure) and a series of additional holes arranged on the carbon fiber tube (measuring static pressure) were used to determine the approximate

dynamic pressure at the probe tip. The two horizontally-opposed circumferential holes are arranged to produce a pressure difference which changes with the horizontal angle of the wind vector relative to the probe axis. Similarly, the two vertically-opposed circumferential holes were arranged to produce a pressure difference which changes with the horizontal angle of the wind vector relative to the probe axis. Prior to installation on the HiDRON H2, the probe was calibrated in a wind tunnel using an apparatus designed to pitch and yaw the probe at angles up to $25°$ relative to the mean wind vector.

The probe used on these flights was also heated to prevent ice formation within the probe during flight. This was accomplished by wrapping the probe body in nickel-chromium resistance wire. A feedback circuit, using a thermistor attached to the probe tip, passed current through the wire at a rate sufficient to maintain the probe tip temperature at $50°C$. Comparison of calibrations with and without heating active indicated that there was no influence of probe heating on the five-hole-probe response characteristics.

Each hole on the probe was connected to differential pressure transducers through 1.75 mm diameter flexible polymer tubing. To ensure that the low-density conditions at flight altitude did not result in pressure differences below the sensitivity of an individual transducer, measured pressure difference was converted to analog voltage using two different sets transducers by teeing the tubing to each transducer sets. The low sensitivity transducer set was comprised of TE Connected Measurements 4515-DS5A002DP differential pressure transducers with a 500 Pa range. The second transducer set was comprised of Allsensors DS-0368 differential pressure transducers with a 65 Pa range. Both sets of analog output voltages were linearly scaled relative to the maximum transducer range with a nominal span of 4.5V and 4.0V respectively. Note that the during flight, the autopilot maintained flight speeds sufficient to produce pressure differences well within the range of the low-sensitivity transducers and hence only the readings from these sensors were used for this analysis.

Based off of established procedures, e.g. as outlined by Treaster and Yocum (1978), Wildmann et al. (2014), Bohn and Simon (1975) and van den Kroonenberg et al. (2008), the pressure differences at each yaw and pitch angle combination were used to build pressure coefficients

$$C_\beta = \frac{\Delta P_{32}}{\Delta P_1 + 0.5(\Delta P_{32} + \Delta P_{54})} \tag{2a}$$

$$C_\alpha = \frac{\Delta P_{54}}{\Delta P_1 + 0.5(\Delta P_{32} + \Delta P_{54})} \tag{2b}$$

$$C_q = \frac{\Delta P_1 - Q}{\Delta P_1 + 0.5(\Delta P_{32} + \Delta P_{54})} \tag{2c}$$

where ΔP_1 is the pressure difference between the central hole and the static pressure, ΔP_{32} is the pressure difference across the horizontal probe holes, ΔP_{54} is the pressure difference across the vertical probe holes and Q is the dynamic pressure. The probe design resulted in unique combinations of C_α and C_β for each yaw and pitch angle of the probe relative to the wind vector,

with the relationship between C_α and C_β determined via wind-tunnel calibration. The same calibration procedure was used to determine the relationship between C_q and Q. To analyze the flight data, C_α and C_β were calculated for every measurement point and the unique combination used to determine the wind vector angle relative to the probe axis. The corresponding value of C_q measured at that relative angle allowed Q to be determined from the measured ΔP_1. The result is knowledge of the magnitude and direction of the dynamic pressure vector relative to the probe axis. This is then converted to velocity using the density determined from iMet-XF measurements of the ambient pressure, temperature and humidity.

To convert the velocity vector magnitude and direction relative to the aircraft into a frame of reference relative to the ground, an additional coordinate transformation was conducted using the aircraft's pitch, yaw, and roll angles as measured by the autopilot. Details of this process are provided in Witte et al. (2017) and are based off of procedures described in Lenschow (1972) for measurements using similar probes mounted on crewed aircraft. The resulting time-dependent velocity vector is described using components $u(t)$, $v(t)$, and $w(t)$ which are aligned to the east, to the north, and up, respectively. The time-dependent horizontal velocity magnitude and direction were then found from

$$U(t) = \left(u(t)^2 + v(t)^2\right)^{-0.5} \tag{3}$$

and

$$dir(t) = \operatorname{atan2}\left(-u(t), -v(t)\right) \tag{4}$$

where atan2 indicates a numerical implementation of the $\tan^{-1}$ function used to disambiguate the polar direction using the quadrant formed by the sign of the velocity components.

Note that in order to perform the transformation to the earth-fixed frame of reference, the aircraft position and orientation information was up-sampled from the autopilot's 10 Hz sample rate to the 1 kHz sample rate used by the on-board data acquisition system, with the up-sampling conducted using simple linear interpolation. Note also that, although data was acquired at a 1 kHz sample rate, the actual probe response was estimated to be on the order of 10 Hz (Witte et al., 2017) due to attenuation within the tubing connecting the probe to the transducers coupled with resonance within the probe cavities.

Finally, it should be mentioned that a pressure line disconnected disconnected prior to Flights 2 and 3, requiring the conversion of five-hole probe voltages to wind for these flights to take a slightly different approach whereby the probe-aligned velocity component was combined with the aircraft slideslip angle to infer horizontal wind components. The vertical velocity component was processed as per Flight 1.

2.3.2 Infrasonic Microphone:

A property of infrasound particularly favorable to the objectives of the proposed work is that it propagates over long distances with little attenuation. Hence, infrasonic measurements of acoustic frequencies below 20 Hz were conducted using an infrasonic microphone. For these tests an extremely low frequency microphone and acoustic measurement system developed at NASA

Langley Research Center (LaRC) was used. The microphone, shown in Fig. 2b, was capable of infrasound detection in a portable and easily deployable form factor. Low bandwidth and high sensitivity of the microphone was realized through a high diaphragm compliance (low diaphragm tension) and a large diaphragm radius. The geometry of the microphone was designed

205 such that membrane motion was substantially critically damped and optimally dimensioned for the 0.01 Hz to 20 Hz frequency range. A signal-conditioning unit amplified the microphone output to a ± 10 V full-scale output.

2.3.3 Data Acquisition:

A Measurement Computing Systems MCC USB-1608FS-Plus data acquisition system (DAQ) was used to digitize the voltage output from the six pressure transducers and microphone signal conditioning unit. This particular unit was capable of recording

210 8 single-ended analog inputs simultaneously at 16-bit resolution at rates of up to 400 kHz. During these experiments the DAQ sampled 7 channels containing the pressure transducer and infrasonic microphone analog voltage signals at 1 kHz for each channel, sending the resulting digitized values to the embedded computer for logging. The DAQ also provided the 5 V signal used to power the pressure transducers.

2.3.4 Embedded Computer:

215 The DAQ was connected via universal serial bus (USB) to a mini stick computer with an Intel Atom Z8350 processor, 128GB eMMC non-volatile memory, and 4GB RAM. To minimize RF interference and shield the computer from high altitude radiation, the computer was encased in a copper shield (Fig. 3c). A custom script was used to control data acquisition and storage. The computer stored all recorded data on its eMMC memory which was then downloaded post-flight via the USB connection for archiving and further analysis. To allow payload operational verification, an RS232 connection was established between

220 the computer and the autopilot. Through this channel, sensor voltage variance and preliminary turbulence detection parameters were passed to the autopilot to be included in the telemetry stream. This information was later available for temporal alignment of sensor and autopilot data, which were logged separately.

2.4 Flight Profiles:

The flight trajectories for all three flights are presented in Fig. 4. The flight profiles encompassed balloon launch, ascent to

225 25 km or 30 km altitude at an ascent rate of approximately 7 m s^{-1}, before release of the HiDRON H2 aircraft. Once released, the HiDRON H2 conducted a controlled return to the airspace above the launch and control point, whereby it began a spiraling descent at an initial radius of approximately 5 km. As the aircraft descended, this radius was reduced to approximately 4 km and eventually, once within the boundary layer, 1 km to keep the aircraft close to the designated landing point. During the descent phase of the flight, the rate of descent decreased from 5 m s^{-1} to 1 m s^{-1} (producing a nominal descent rate of 2 m s^{-1}).

230 Overall flight time was approximately 6 hours with 4 hours of that being the descent phase. Controlled landing and recovery occurred on the Spaceport America main runway at which point the aircraft, payload and all logged data were recovered.

All three flights started in the morning hours, with Flight 1 launched at 13:47 UTC on June 1 2021, released from the balloon at 14:35 UTC, and landing at 18:42. Flight 2 launched at 14:04 UTC on June 4 2021, released at 15:15 UTC and landed at 18:39. Finally, Flight 3 launched at 14:07 UTC on June 6 2021, released at 15:17 UTC, and landed at 19:43. Local time at
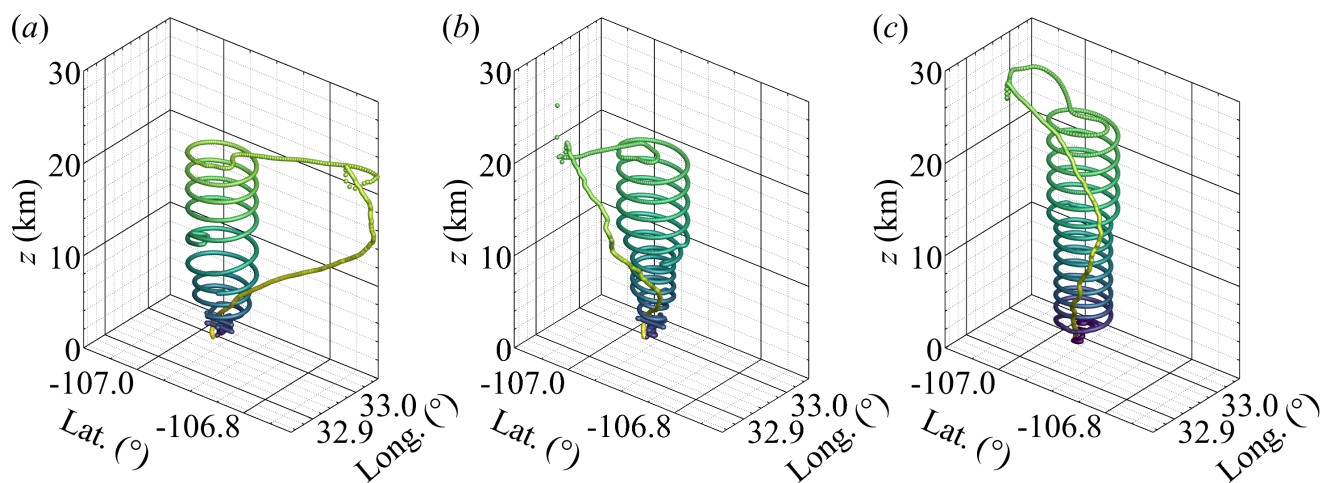235 Spaceport America was Mountain Daylight Time (MDT -6:00).

Figure 4. HiDRON H2 flight trajectory for (a) Flight 1, (b) Flight 2 and (c) Flight 3. Trajectory is colored by time, with lighter color indicating earliest phase of balloon ascent. z indicates height above ground level (a.g.l.)

3   Results

In this section, we present and discuss selected statistics determined from the measured values of temperature, relative humidity, wind vector, and infrasonic microphone signal amplitude. These statistics are presented in the form of vertical profiles in Sections 3.1 to 3.3, and in the form of spatial distributions in Section 3.4. Due to the configuration of the sensors on the aircraft,
240 only data from the controlled descent phase of the flight was found to provide reliable results and thus only measurements from the descent are presented in this section. In addition, z is used to indicate altitudes are referenced to ground level, i.e. above ground level (a.g.l.). To obtain statistical properties as a function of z, the time-series during descent was divided into 30 s long segments representing horizontal distances of approximately 600 m (varying from 300 m to 2420 m) and vertical distances of 60 m (varying from 150 m to 30 m). Quantities averaged over these 30 s segments are indicated using $\langle\,\rangle$ brackets.

245 ### 3.1   Mean quantities

To establish the ambient conditions during each flight, pressure P, temperature, T, and relative humidity, RH, measured using the HiDRON H2's iMet-XF sensor were combined with horizontal wind magnitude, U, and direction, dir, determined from the five-hole probe measurements. These quantities were averaged over 30 s segments and allow validation of the HiDRON H2 measurements by comparison to the the National Weather Service (NWS) radiosonde weather soundings launched from El

250 Paso, Texas at 12:00 UTC on the same day as each flight. To do so, vertical profiles of $\langle T \rangle$, $\langle RH \rangle$, $\langle U \rangle$ and $\langle dir \rangle$ values are compared to the radiosonde profiles for all three flights in Fig. 5.

With the exception of RH, and within the boundary layer, these quantities show good agreement between the HiDRON H2 and radiosonde data to within 10% of the value measured by the radiosonde. The profiles of temperature (Fig. 5a,c,e) also allow identification of the altitudes and properties of the troposphere, tropopause and stratosphere during each flight. The

255 boundary layer height is also roughly identifiable for altitudes lower than 3 km due to the divergence of the profiles caused by the different time of day between the radiosonde and HiDRON H2 measurements. Above the boundary layer, a constant lapse rate of 8.4 °C km^{-1} was measured throughout the troposphere. Using the temperature gradient as an indicator, the tropopause occurred at $z = 11$ km, above which the temperature continued to decrease with altitude at a rate of 1 °C km^{-1} before the stratospheric temperature inversion creates a positive temperature gradient with a lapse rate of -5.3 °C km^{-1} above an altitude

260 of 19 km.

Similar temperature conditions were also observed for Flight 2 (Fig. 5c), although with a stronger temperature inversion at $z = 13$ km. The lapse rate measured during this flight was 7.9 °C km^{-1} and the tropopause occurred at a slightly higher altitude of $z = 12.5$ km. The temperature gradients in the stratosphere were slightly reduced, with a lapse rate of 1.6 °C km^{-1} until the temperature inversion at $z = 7$ km, above which a gradient of -2.7 °C km^{-1} was measured. A slightly thicker boundary

265 layer was measured for Flight 3 (Fig. 5e), reaching $z = 5$ km due to the later descent for this flight. The tropospheric lapse rate was 8.2 °C km^{-1}, with a slightly higher tropopause measured at $z = 14$ km . Finally, a much lower stratospheric temperature inversion was observed on this flight, located at only $z = 16$ km with a lapse rate of -3.1 °C km^{-1} above and 1.0 °C km^{-1} below this height.

Figures 5b,d,f compare the corresponding RH measurements from both the HiDRON H2 and NWS radiosonde. Significant

270 differences are clearly evident. However, noting that the radiosonde data were obtained from a location 160 km away from the flight location, this is likely due to spatial heterogeneity in the atmospheric moisture concentration. Comparison of cloud height and coverage data retrieved from an Automated Surface Observing System (ASOS) database confirmed that the cloud conditions near Truth or Consequences, NM (near Spaceport America) were different from those measured near El Paso, TX for the same time period.

275 The magnitude and direction of the horizontal winds for all three flights are shown in Fig. 6. Again, the wind magnitude and direction measured by the HiDRON H2 compare well with the radiosonde soundings. The strongest winds occurred during Flight 1, with the winds coming from 270° and increasing with altitude to a peak value over 20 m s^{-1} at the tropopause ($z = 12.5$ km), before decreasing with altitude to the stratospheric inversion near $z = 17$ km. This pattern of constant wind direction and high wind magnitude is consistent with the presence of a jet stream, and the NOAA upper air wind meteorological

280 maps indicate that during Flight 1 a tropical jet stream was centered to the southeast of the flight location, over central Texas, such that the flight path was on the outer edge of the jet. This jet had moved to the east by the time of Flights 2 and 3, which is reflected in the reduced magnitude of winds measured during these flights. The relative position of the jet stream for Flight 1 also explains the slightly higher wind magnitudes measured at El Paso, which was closer to the center of the jet. Above the
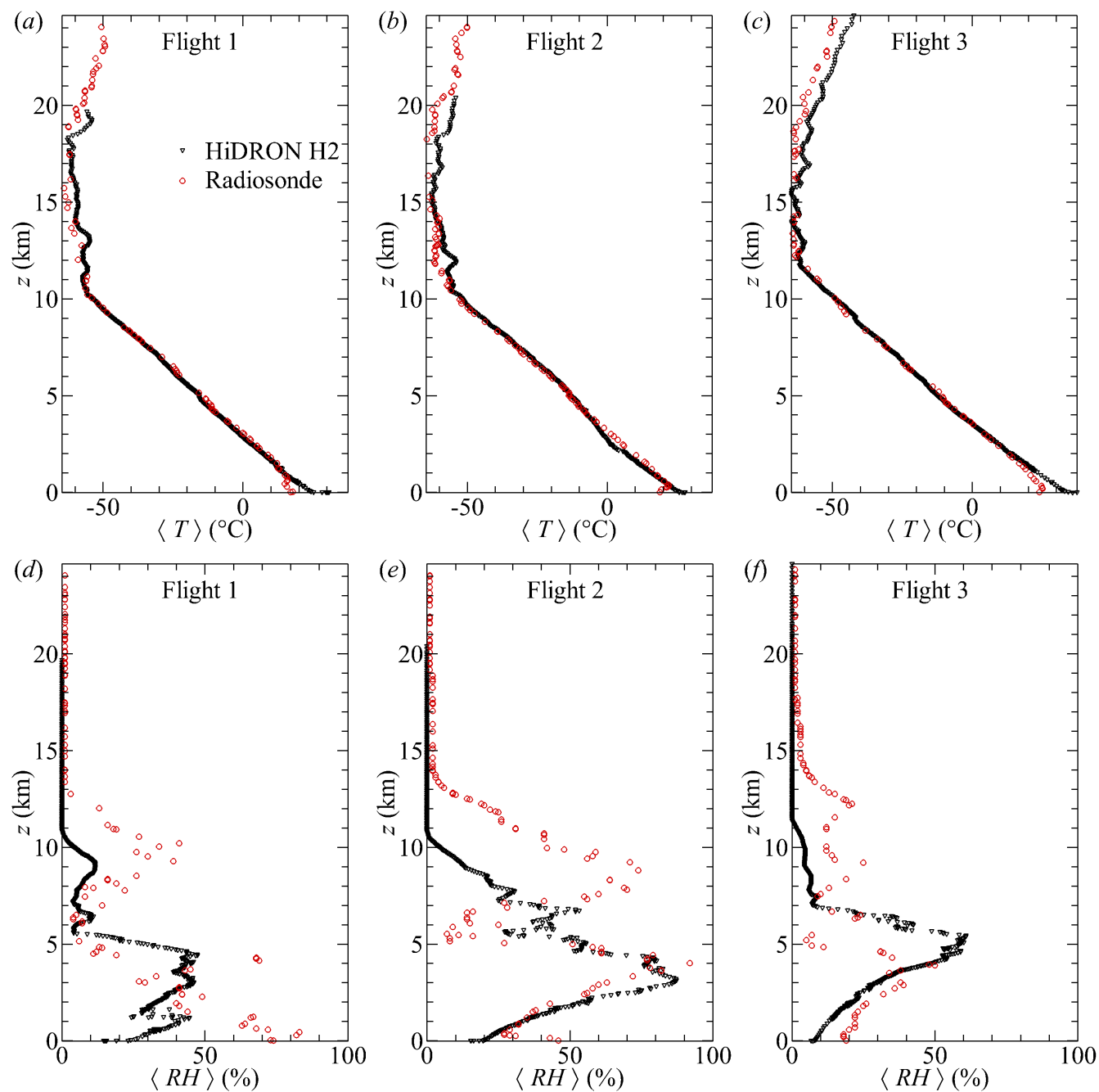
11

Figure 5. Temperature profiles measured during (*a*) Flight 1; (*b*) Flight 2; and (*c*) Flight 3. Corresponding relative humidity profiles shown for (*d*) Flight 1; (*e*) Flight 2; and (*f*) Flight 3. Solid black symbols indicate HiDRON H2 measurements, and open red symbols indicate radiosonde soundings.
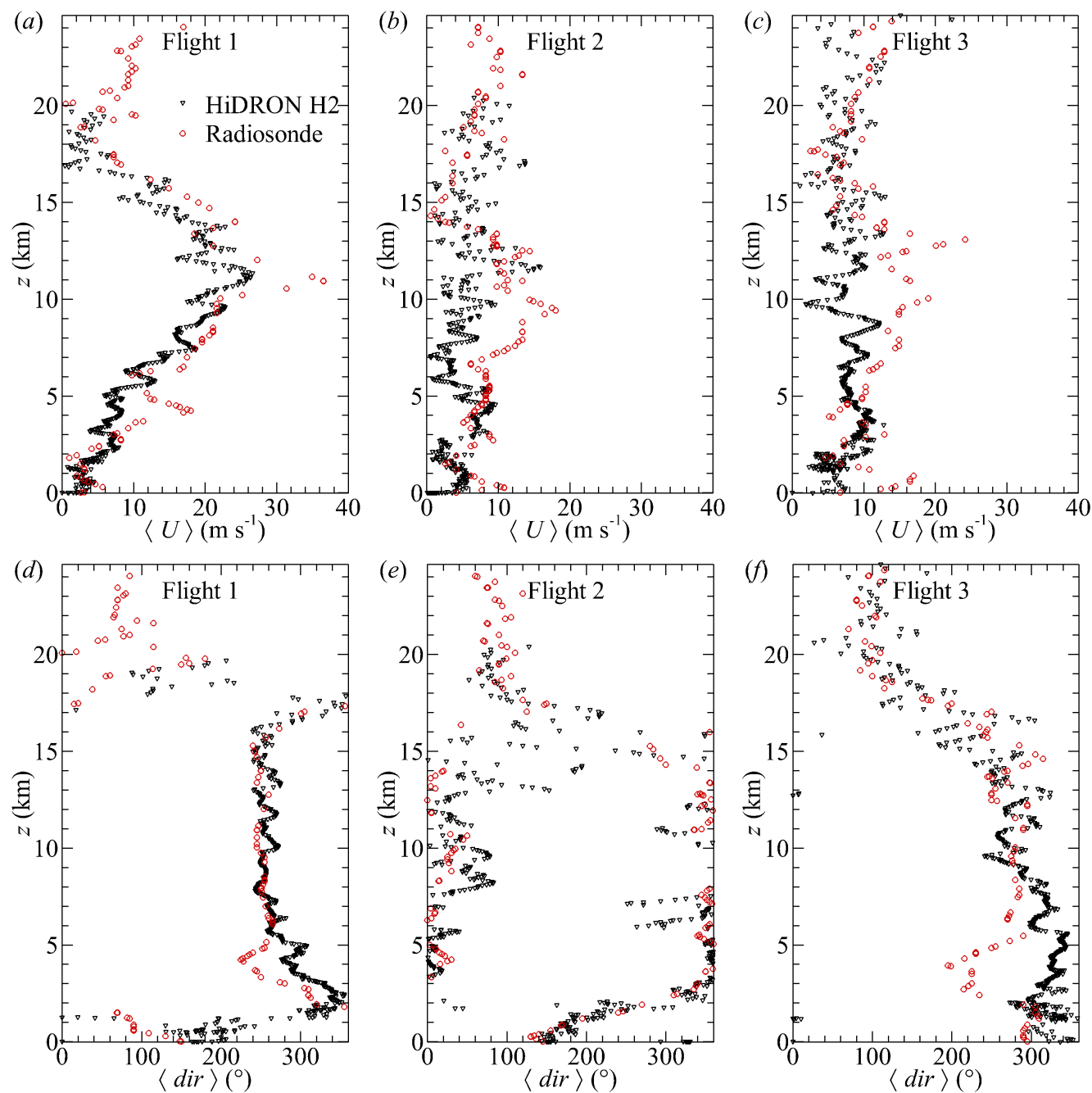
Figure 6. Horizontal wind magnitude a measured during (*a*) Flight 1; (*b*) Flight 2; and (*c*) Flight 3. Corresponding wind direction shown for (*d*) Flight 1; (*e*) Flight 2; and (*f*) Flight 3. Solid black symbols indicate HiDRON H2 measurements, and open red symbols indicate radiosonde soundings.

jet stream, the winds increase with altitude again, with significant directionality shifts indicating multiple shear layers were

285   present above the temperature inversion.

As noted, calmer wind conditions were observed during Flights 2 and 3 (Fig. 6b,c and Fig. 6e,f respectively) with magnitudes typically below $U = 10$ m s^{-1}, consistently from the north for $z < 15$ km for Flight 2, with directional shear observed between $z = 15$ km and $z = 20$ km. Finally, observations during Flight 3 indicate nearly constant values of $U \approx 10$ m s^{-1} up to $z = 30$ km, with winds coming from $300°$ in the troposphere with backing with altitude to be from $100°$ at $z = 20 \ km$
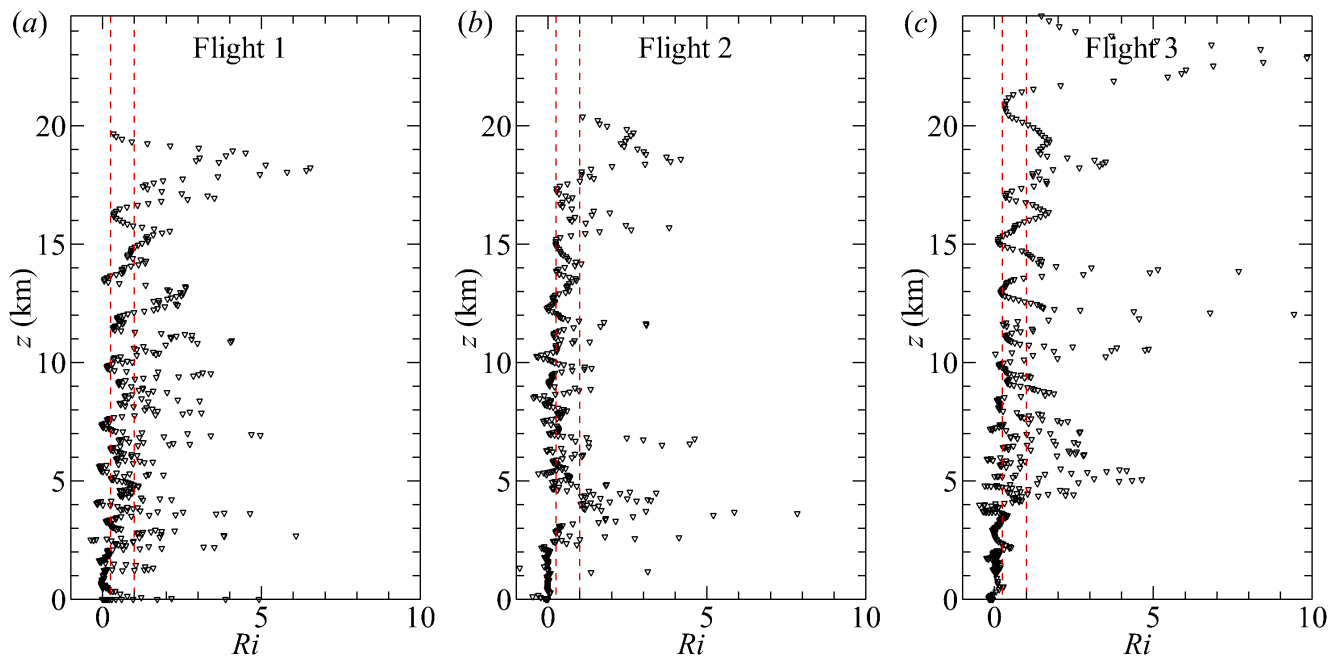

Figure 7. Gradient Richardson number, Ri, profiles for (a) Flight 1; (b) Flight 2; and (c) Flight 3. The vertical lines represent a critical Richardson number range between of $Ri = 0.25$ and $Ri = 1$.

290   The corresponding gradient Richardson number, Ri, provides some perspective of the resulting atmospheric stability conditions. To calculate Ri, the 30 second average of virtual potential temperature, $\langle \theta_v \rangle$, was first calculated using

$$\langle \theta_v \rangle = \left\langle T \left(\frac{100000}{P} \right)^{0.2861} (1 + 0.61q) \right\rangle \tag{5}$$

where q is the water vapor mixing ratio, T is the temperature in Kelvin and P is the pressure in pascals. Vertical gradients of $d\langle \theta_v \rangle / d\langle z \rangle$ and longitudinal and latitudinal components of wind, $d\langle u \rangle / d\langle z \rangle$ and $d\langle v \rangle / d\langle z \rangle$ respectively, were calculated using

295   central differencing. To minimize the influence of small-scale fluctuations and instrumentation noise on the calculation, an additional smoothing process was applied using a localized regression fit applied over 5 successive 30 second intervals. These

quantities were then used to calculate Ri following

$$Ri = \frac{\frac{g}{\langle \theta_v \rangle} \frac{d\langle \theta_v \rangle}{d\langle z \rangle}}{\left(\frac{d\langle u \rangle}{d\langle z \rangle}\right)^2 + \left(\frac{d\langle v \rangle}{d\langle z \rangle}\right)^2} \tag{6}$$

where the gravitational acceleration was approximated using

$$300 \quad g = 9.80665 \frac{R_E}{R_E + z} \tag{7}$$

with $R_E = 6371$ km. Here we assume the critical Richardson number takes on a value somewhere in the range $0.25 < Ri < 1$ (Abarbanel et al., 1984; Galperin et al., 2007).

The Ri profile for Flight 1 is shown in Fig. 7a and indicates the presence of several local regions of instability, appearing on the profiles as multiple thin layers of Ri frequently dipping below values between $Ri = 0.25$ and $Ri = 1$ interspersed with
305 layers of increased stability indicated by $Ri > 1$. The weighting of the measurements towards low Ri indicates that marginally unstable conditions existed in the troposphere during this flight. Above $z = 10$ km the weighting of the Ri profiles towards higher values suggest more stable conditions were present in the stratosphere, with thin regions of potential instability at altitudes of $z = 12$ km, 13 km, and 16 km. The Ri profiles for Flights 2 and 3 shown in Fig. 7b,c are similar, indicating a marginally unstable tropopause, with Flight 2 potentially having slightly higher tropospheric instability than the other two
310 flights. For Flight 3, the thicker boundary layer is evident as a consistently low Ri values up to $z = 4$ km, reflecting conditions corresponding to the more well-developed convective boundary layer were present as the HiDRON H2 passed through the boundary layer later in the day.

3.2 Turbulence Quantities

The results presented in the previous section demonstrated that the stability conditions were sufficient for the production of
315 turbulence during all three flights. Specifically, the Ri results indicate conditions conducive to buoyant turbulent production within the boundary layer, and a conditionally unstable troposphere suggesting the possibility of localized buoyant production was possible in that atmospheric layer. Furthermore, during Flight 1, significant wind shear was measured in the stratosphere, suggesting the potential for mechanical production in the stratosphere.

These properties, however, indicate only that the conditions were present favorable to the production of turbulence. The
320 nature of the HiDRON H2 measurements allows the determination of different metrics that can be used to confirm the presence of turbulence at different altitudes. One measure of the local turbulence intensity is the turbulent kinetic energy, k. Here, k was calculated as a function of distance along the flight trajectory using

$$k = \frac{1}{2}\left(\langle u'^2 \rangle + \langle v'^2 \rangle + \langle w'^2 \rangle\right) \tag{8}$$

where, $u'(t) = u(t) - \langle u \rangle$, with equivalent definitions for $v'(t)$ and $w'(t)$. Note that since $u(t)$, $v(t)$ and $w(t)$ were oversampled, to minimize the influence of high frequency noise on these quantities, $\langle u'^2 \rangle$, $\langle v'^2 \rangle$ and $\langle w'^2 \rangle$ were calculated by first subtracting $\langle u \rangle$, $\langle v \rangle$ and $\langle w \rangle$ from u, v and w, respectively, then calculating the frequency spectrum for each 30 s segment of the time series (here denoted as $F_{uu}(f)$, $F_{vv}(f)$ and $F_{ww}(f)$ respectively, where f is frequency). This was done using Welch's periodogram method implemented with a Hanning window. The low-pass filtered estimates of $\langle u'^2 \rangle$, $\langle v'^2 \rangle$ and $\langle w'^2 \rangle$ were then determined by integrating the resulting spectrum for $f < 5$ Hz. Example spectra of $F_{uu}(f)$ are provided in Fig. 8 and the resulting profiles of k for all three flights are presented in Fig. 9a-c.
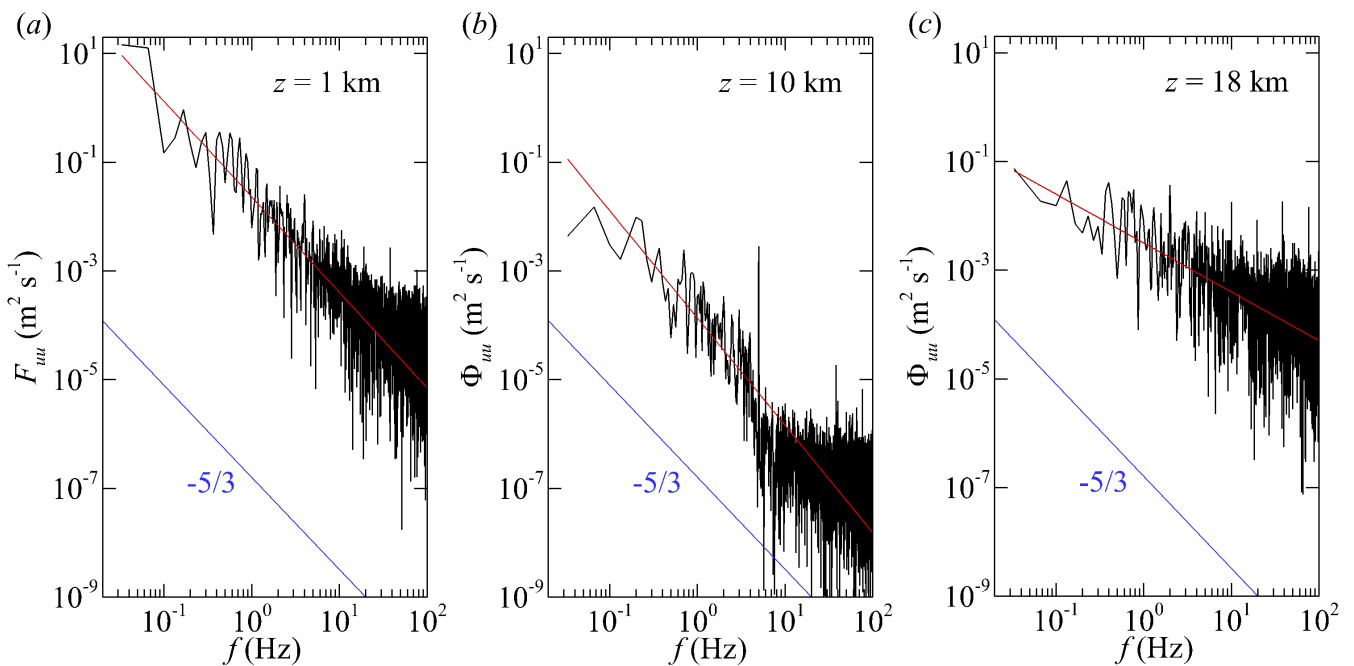

Figure 8. Example energy spectrum calculated from u component of velocity from Flight 1 at (*a*) $z = 1$ km, (*b*) $z = 10$ km, and (*c*) $z = 18$ km. Red lines indicate fit over $f < 5$ Hz range, blue lines indicate $f^{-5/3}$ slope.

For Flight 1 the boundary layer is clearly evident in Fig. 9a as an increase in k for $z < 2$ km, with slightly thicker boundary layers observed in Fig. 9b and c for $z < 4$ km and $z < 3$ km for Flights 2 and 3. Above the boundary layer, the values of k largely remained close to 0 except in several localized regions where elevated k values were measured. For Flight 1 within the troposphere, these regions occurred at $z \approx 6$ km and $z \approx 8$ km, whereas within the stratosphere broadly elevated values of k were observed for $z > 16$ km, with significant increase in k observed at $z = 13$ km and $z = 11.5$ km. Similar behavior was measured during Flights 2 and 3, although the regions of elevated k appear at different altitudes. Note that the elevated values of k may not necessarily correspond to velocity fluctuations caused by turbulence, as evident in Fig. 8c, which shows that, although the spectra indicate a broadband energy content within the five-hole-probe sensor's response range ($f < 10$ Hz), the spectra display a significant deviation from the characteristic $-5/3$ slope associated with the locally isotropic turbulence
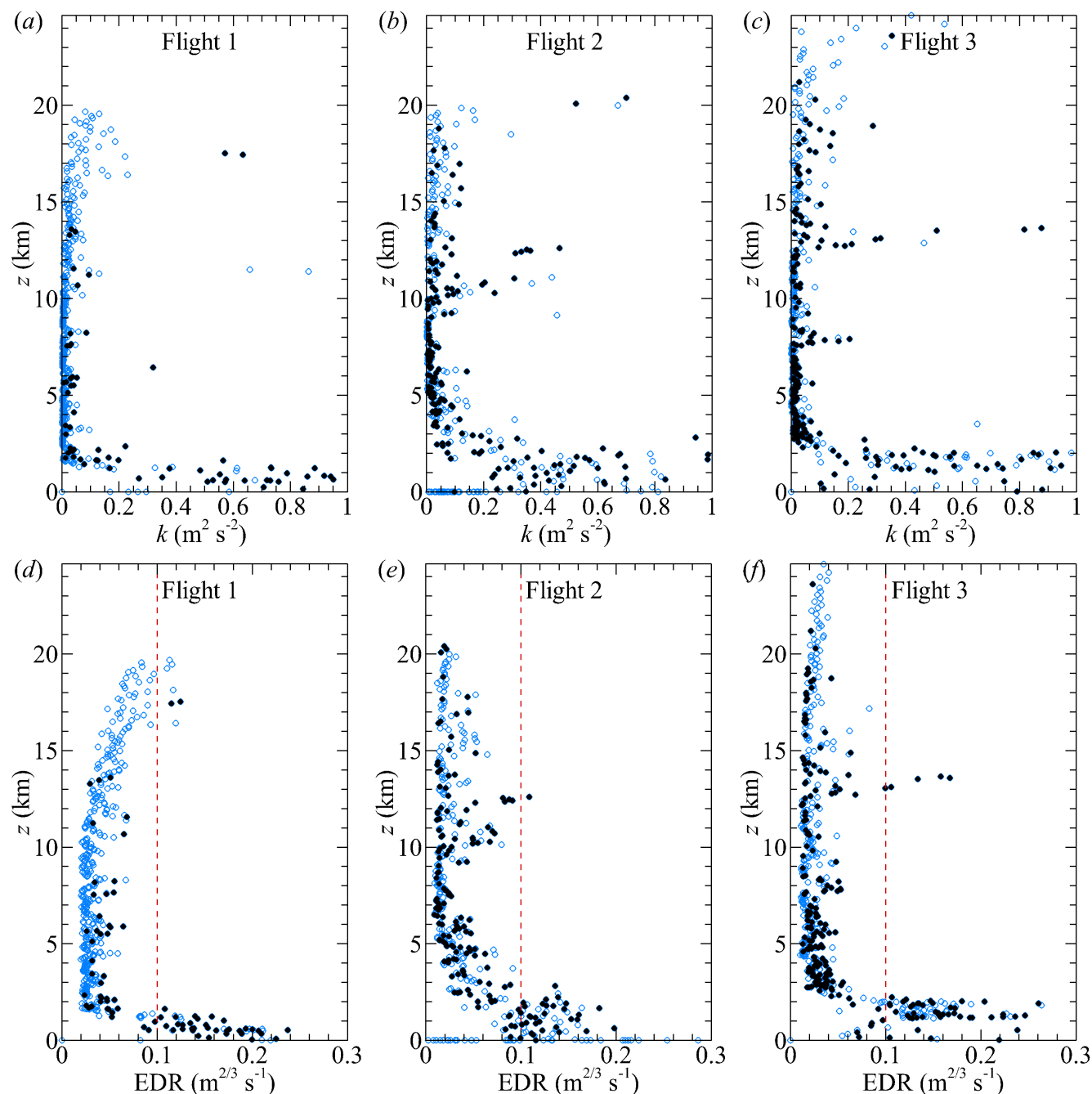
Figure 9. Profiles of k for (*a*) Flight 1, (*b*) Flight 2, and (*c*) Flight 3. Corresponding profiles of EDR are shown for (*d*) Flight 1, (*e*) Flight 2, and (*f*) Flight 3. Solid black symbols indicate measurements where $-1.8 < n < -1.5$. Dashed lines indicate qualitative turbulence intensity levels from Huang et al. (2019) referred to as: steady for $EDR < 0.1$; weak for EDR between 0.1 and 0.3; moderate for EDR between 0.3 and 0.5; strong for EDR between 0.5 and 0.8; and very strong for $EDR > 0.8$.

340 expected within the inertial subrange (Kolmogorov, 1941). When instances where the power law fit of Bf^n to $F_{uu}(f)$ in the range of $f < 5$ Hz which produced exponent values within the range of $-1.8 < n < -1.5$ are isolated (as indicated by solid black symbols in Fig. 9) these turbulent regions become more localized for Flight 1. However, for Flights 2 and 3 (Fig. 9b and c) this criteria becomes less discriminating, which may correspond to more active atmospheric turbulence conditions during these flights. Note that for all three flights a layer of high k was observed in a region near the tropopause. This will later be

345 shown to correspond to the presence of gravity waves and tropopause folding formed by breaking Kelvin waves (Shapiro, 1980; Fujiwara et al., 2003).

Note that due to the time averaging used, the value of k will only incorporate contributions from relatively short wavelengths, corresponding to the distance travelled by the aircraft during the averaging time. Although the horizontal velocity of the aircraft was somewhat altitude dependent, for these flights the longest wavelength of velocity fluctuation incorporated in the

350 k measurement would be on the order of 300 m. An additional metric that can be used to quantify turbulence is the turbulent kinetic energy dissipation rate, ε. As ε tends to scale with the rate of production and magnitude of k, it is often used to quantify the turbulence intensity. This is particularly useful as ε can be determined from small-scale fluctuations and therefore does not require resolution of the largest scales of turbulence while providing a measure of the turbulence intensity over all wavelengths.

As direct measurement of ε requires measurement of spatial gradients of velocity over distances on the order of the Kol-

355 mogorov scale, direct measurement in the atmosphere is challenging. Thus, an indirect estimate of ε is usually employed. Here, we assume the presence of sufficiently high Reynolds number for the formation of an inertial subrange in the energy spectrum. Under such conditions, the one-dimensional wavenumber spectrum in the inertial subrange is expected to follow a scaling such that

$$\Phi_{11}(\kappa_1) = 0.49\varepsilon^{2/3}\kappa_1^{-5/3} \tag{9}$$

360 where κ_1 is a component of the wavenumber vector and Φ_{11} is the energy spectrum for the velocity component parallel to κ_1 (Pope, 2000). For the present measurements, this scaling was used to estimate ε by first rotating the u, v, w coordinate system from the east-north-up alignment to instead align u with an axis parallel to the horizontal flight direction, i.e. u_1. This direction was determined by averaging the aircraft's horizontal ground velocity over a 30 second segment of time and determining the relative angle of the flight path with respect to east. The frequency spectrum of u_1, $F_{11}(f)$, was then calculated on the

365 rotated wind velocity vector following the same procedure used to calculate $F_{uu}(f)$. The longitudinal wavenumber was then approximated using Taylor's frozen-flow hypothesis such that $\kappa_1 \approx 2\pi f \, V^{-1}$, where V is the magnitude of the aircraft's ground speed, again averaged over the 30 s time segment. The result is such that $\Phi(\kappa_1) \approx V(2\pi)^{-1}F(2\pi f \, V^{-1})$. Finally, a power-law, i.e. $A\kappa_1^n$, was fit to the resulting spectrum over the κ_1 range corresponding to $f < 5$ Hz, thus allowing the estimate

$$\varepsilon = \left(\frac{A}{0.49} \left(\frac{2\pi f}{V} \right)^{5/3} \right)^{3/2} \tag{10}$$

370 to be made for each 30 s time segment.

Note that the corresponding statistic of eddy dissipation rate, $EDR = \varepsilon^{1/3}$, is often used in the aviation industry to quantify turbulence. Qualitatively, the turbulence can be referred to as: steady for $EDR < 0.1$; weak for EDR between 0.1 and 0.3; moderate for EDR between 0.3 and 0.5; strong for EDR between 0.5 and 0.8; and very strong for $EDR > 0.8$. Hence, here we use EDR to describe the turbulent kinetic energy dissipation rate as it allows a qualitative comparison of turbulence intensity to established thresholds. Profiles of EDR are shown for all three flights in Fig. 9d-f. Note that the approach used to determine ε will provide a non-zero value even if no turbulence is present, and therefore some caution is required when interpreting these EDR profiles beyond being a qualitative indication of the presence of turbulence in the form of localized regions of relatively high EDR. To provide some additional discrimination, as with k, we indicate measurement points when $-1.8 < n < -1.5$ using solid black symbols.

As could be expected, regions of high EDR correspond to regions with high k, although the profiles have different characteristics for these two quantities. For example, the EDR indicates that the aircraft experienced turbulence during Flight 1 (Fig. 9c) within the boundary layer ($z < 3$ km) and within the stratosphere ($z > 18$ km), although the high k region measured at $z = 11$ km does not appear to be turbulence according to the EDR metric. That said, for Flights 2 and 3, there was better correspondence between EDR and k, with the most active regions appearing in the boundary layer and tropopause. Interestingly, the EDR shows generally enhanced values in the stratosphere for Flight 1, which does not correspond to indications of the presence of a classical inertial subrange with $\kappa_1^{-5/3}$. It will be shown later that this enhanced EDR corresponds to measured fluctuations in velocity introduced by the presence of gravity waves at these altitudes.

3.3 Infrasonic Detection of Turbulence

As noted in Section 1, a primary objective of these experiments was to determine the effectiveness of infrasonic sensing for detecting atmospheric turbulence. Here, we use the amplitude of the acoustic signature quantified using its variance, σ_{IS}^2. Here, σ_{IS}^2 was calculated by integrating energy spectra from the time series of microphone signal for each 30 s increment and integrating these spectra over a frequency range of $f < 10$ Hz. This process produces a measure of the amplitude of the infrasonic frequency content between 0.03 Hz and 10 Hz for each 30 s segment. Some sensitivity of σ_{IS}^2 was observed to both the frequency range and time increment used for its calculation, with the range used selected due to finding that lower frequency acoustic content better correlated with the EDR values measured with the five-hole-probe when compared to the higher frequency acoustic content, which tended to contain additional signal noise.

Profiles of σ_{IS}^2 are shown for all three flights in Fig. 10. Noticeably, there was a decrease in signal amplitude with altitude measured in all cases. It was found that this decrease closely corresponds to the reduction in local atmospheric pressure, and therefore this decrease is expected to be caused by the increased acoustic attenuation corresponding to the increase in molecular mean free path with altitude. Despite this attenuation, localized increases in σ_{IS}^2 were observed, particularly within the boundary layer, providing an initial confirmation of the presence of infrasonic sound generation by turbulence. Additional localized increases at higher altitudes were also measured, for example during Flight 1 around $z = 4$ km and around $z = 8$ km which may correspond to acoustic generation by turbulence in the troposphere, but these altitudes did not directly align with
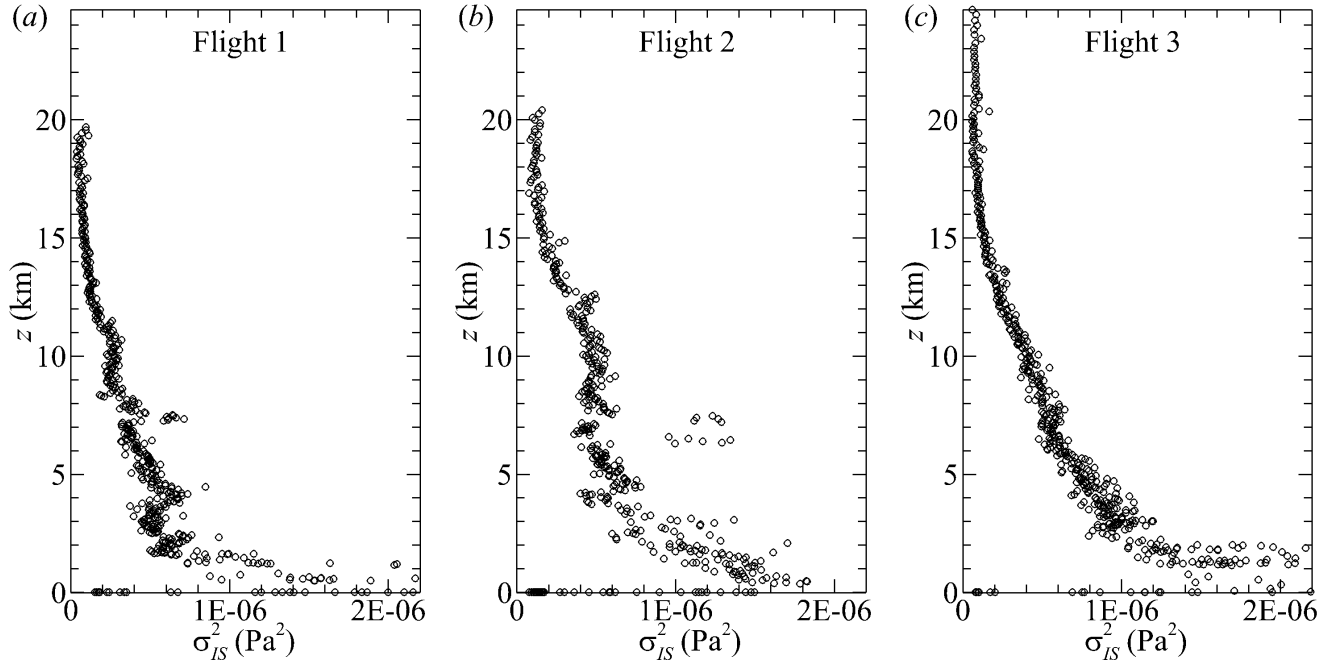
Figure 10. Infrasonic signal amplitude, σ_{IS}^2, profiles measured during (*a*) Flight 1, (*b*) Flight 2, and (*c*) Flight 3.

altitudes of increased turbulence in the corresponding profiles of k and EDR. The relationship between σ_{IS}^2 and EDR will be
405   examined in more detail in the next section.

3.4 Horizontal Structure of Turbulent Regions

A rough comparison between the measurements of k and EDR, shown in Fig. 9, to the estimates of Ri, shown in Fig. 7,
shows that layers of regions of turbulence closely correspond to regions of Ri and hence low buoyant stability. For example,
as measured during Flight 1 within the boundary layer, and at $z = 6$ km, 11 km and 17 km. However, there are also regions
410   with low Ri evident in Fig. 7 which do not appear to correspond to regions where turbulence was measured. To better compare
these quantities, the measurements of EDR are shown as functions of Ri in Fig. 11. Although this figure shows the expected
behavior of increased EDR corresponding to low Ri, and vice versa, it also shows that there are instances where high EDR
was measured where $Ri > 1$, even for cases where $-1.8 < n < -1.5$.

To investigate these regions more closely, we took advantage of the horizontal flight capability of the HiDRON H2 to
415   expand the vertical profiles along the axis of flight, here represented in the form of angular position of the aircraft relative
to the center of the aircraft's orbit, α, which was defined with $\alpha = 0$ directed to the north and increasing positive towards
the east. To visualize the distribution of different measured quantities along the flight path, the 30 s averaged quantities were
then interpolated onto the resulting α-z plane. Furthermore, to isolate and visualize localized perturbations, we calculated the
average value over a $\Delta z = 1$ km range, e.g. $\overline{\langle \phi \rangle}$ where the overline indicates a bin average of arbitrary variable $\phi(z)$ over the
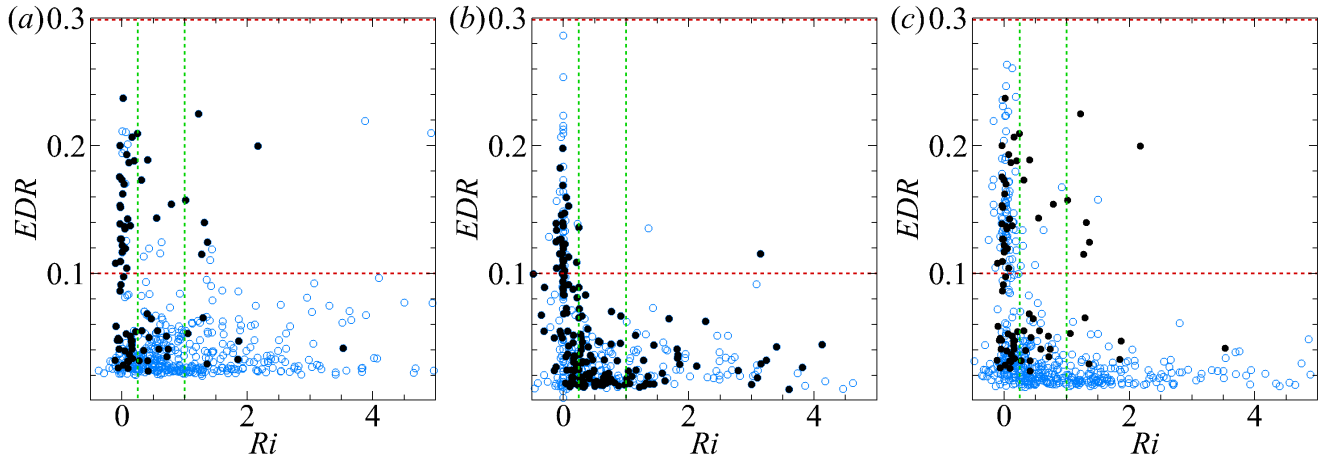
Figure 11. Comparison of measured EDR as a function of Ri for (a) Flight 1, (b) Flight 2 and (c) Flight 3. Solid black symbols indicate measurements where $-1.8 < n < -1.5$. Dashed red lines indicate same qualititative turbulence intensity levels as in Fig. 9 and dashed green line indicates critical Ri range of $Ri = 0.25$ to $Ri = 1$.

420   altitude range $z - 0.5$ km to $z + 0.5$ km. The perturbations were then calculated using

$$\langle \phi(\alpha, z) \rangle' = \langle \phi(\alpha, z) \rangle - \overline{\langle \phi(z) \rangle} \tag{11}$$

where again the $\langle \ \rangle$ brackets indicate a 30 s averaged quantity and the prime indicates a quantity that has undergone the

layer decomposition described by equation 11. In this way, the large-scale perturbations at a particular altitude could be better

identified. Visualizations in the form of contour maps of selected quantities resulting from this process are presented in Figs. 12,

425   13 and 14 for Flights 1, 2 and 3 respectively.

When the measurements are examined in this manner, several interesting features can be identified which provide increased

information about the structure and dynamics of the atmosphere during each flight. Starting first with Flight 1, the distribution

of $\langle T \rangle'$ shown in Fig. 12a reveals the presence of strong temperature oscillations at the tropopoause ($z \approx 10$ km), located in the

southern portion of the orbit ($\alpha > 90°$ and $\alpha < -120°$). These perturbations had a wavelength of approximately 1.5 km and

430   coincide with similar scale oscillations in $\langle w \rangle'$ (shown in Fig. 12b) at the same location and are therefore consistent with the

presence of a gravity wave. Similar, small-scale fluctuations were also measured in the stratosphere ($z > 15$ km) for $\alpha > 45°$

and $\alpha < -120°$ which indicates that the aircraft also flew through a different gravity wave layer at higher altitudes. Interestingly

the $\langle w \rangle'$ distribution in the range $90° < \alpha < 150°$ indicates potential coupling between these layers along this portion of the

flight path, suggesting the possibility of momentum exchange between them.

435   Some indication as to why the behavior was different for the northern portion of the orbit ($-120° < \alpha < 90°$) can be found

when examining the Ri distribution shown in Fig. 12c. This portion of the flight was characterized by a region of stable air in

the stratosphere ($z > 15$ km), that took the form of fingers of unstable and stable air below $z < 15$ km that correspond to rising
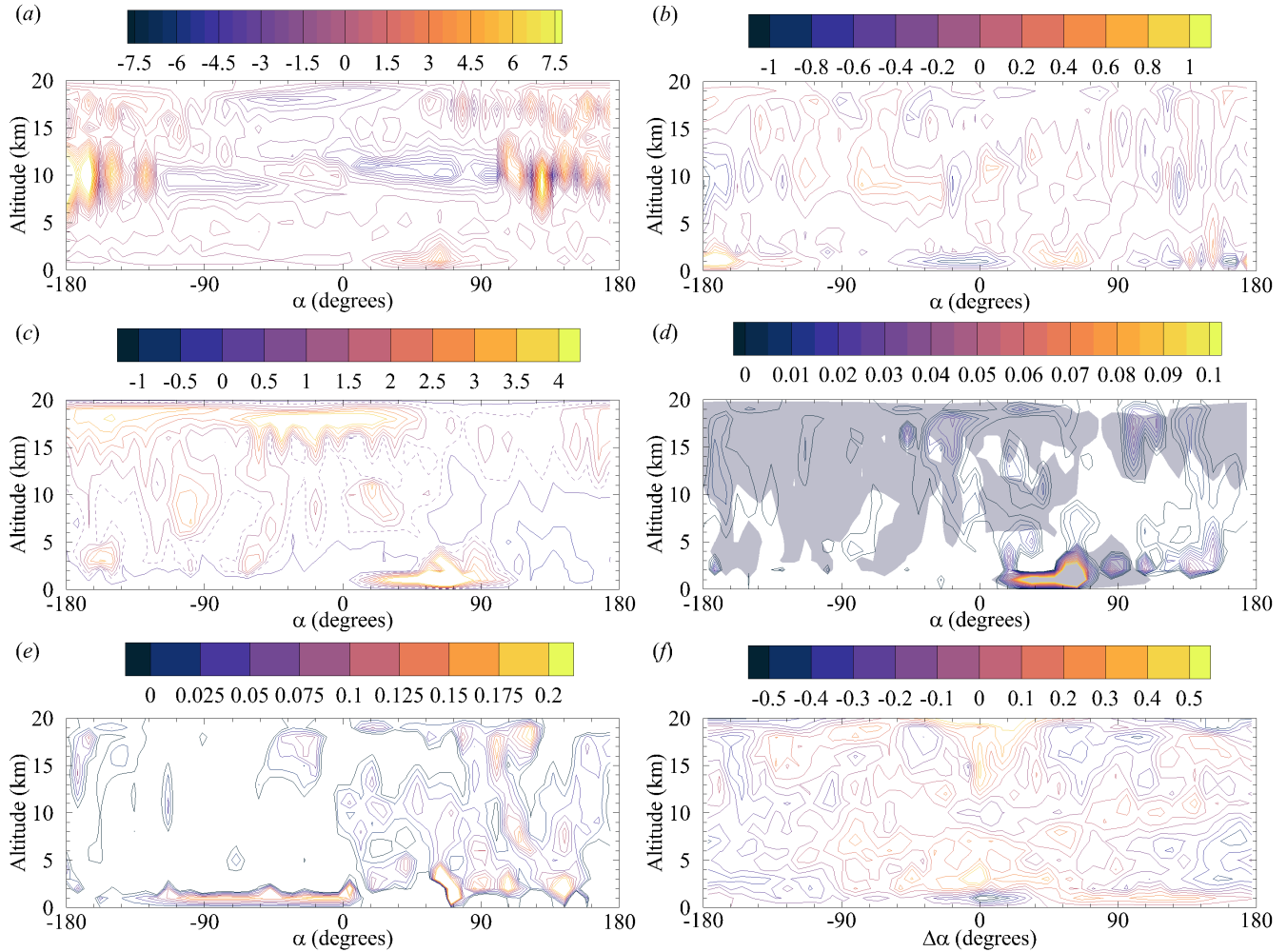
Figure 12. Interpolated values for Flight 1 of: (a) $\langle T \rangle'$ in $°C$; (b) $\langle w \rangle'$ in m s^{-1}; (c) Ri; (d) EDR' in m$^{2/3}$ s^{-1}; (e) $\left(\log_{10} \sigma_{IS}^2\right)'$ in $\log_{10}(Pa^2)$; and (f) $R(\Delta\alpha, z)$, the cross-correlation of EDR' and $\left(\log_{10} \sigma_{IS}^2\right)'$. Dashed lines in (c) and shaded regions in (d) identify the boundary where $Ri = 1$.

($Ri < 1$) and descending ($Ri > 1$) air in Fig. 12b. These vertical perturbations appear to extend throughout the troposphere, indicating the presence of vertical buoyant structures that were not evident in the profiles shown in Fig. 7.

440   The corresponding distribution of turbulence is reflected in the visualization of EDR' shown in Fig. 12d. In this visualization, what appears to be isolated layers of EDR in Fig. 9a can now be identified as having been produced by vertically-aligned structures. In the stratosphere for $z > 15$ km, localized regions of elevated EDR' were measured in the region where the $\langle w' \rangle$ fluctuations suggested coupling between the observed layers of gravitational waves ($80° < \alpha < 130°$). Several vertically aligned regions were also measured in the stratosphere in the range $-45° < \alpha < -45°$ which corresponds to the interface of stable and unstable values of Ri. In both these cases, regions of elevated EDR' were present in stable regions where $Ri > 1$,
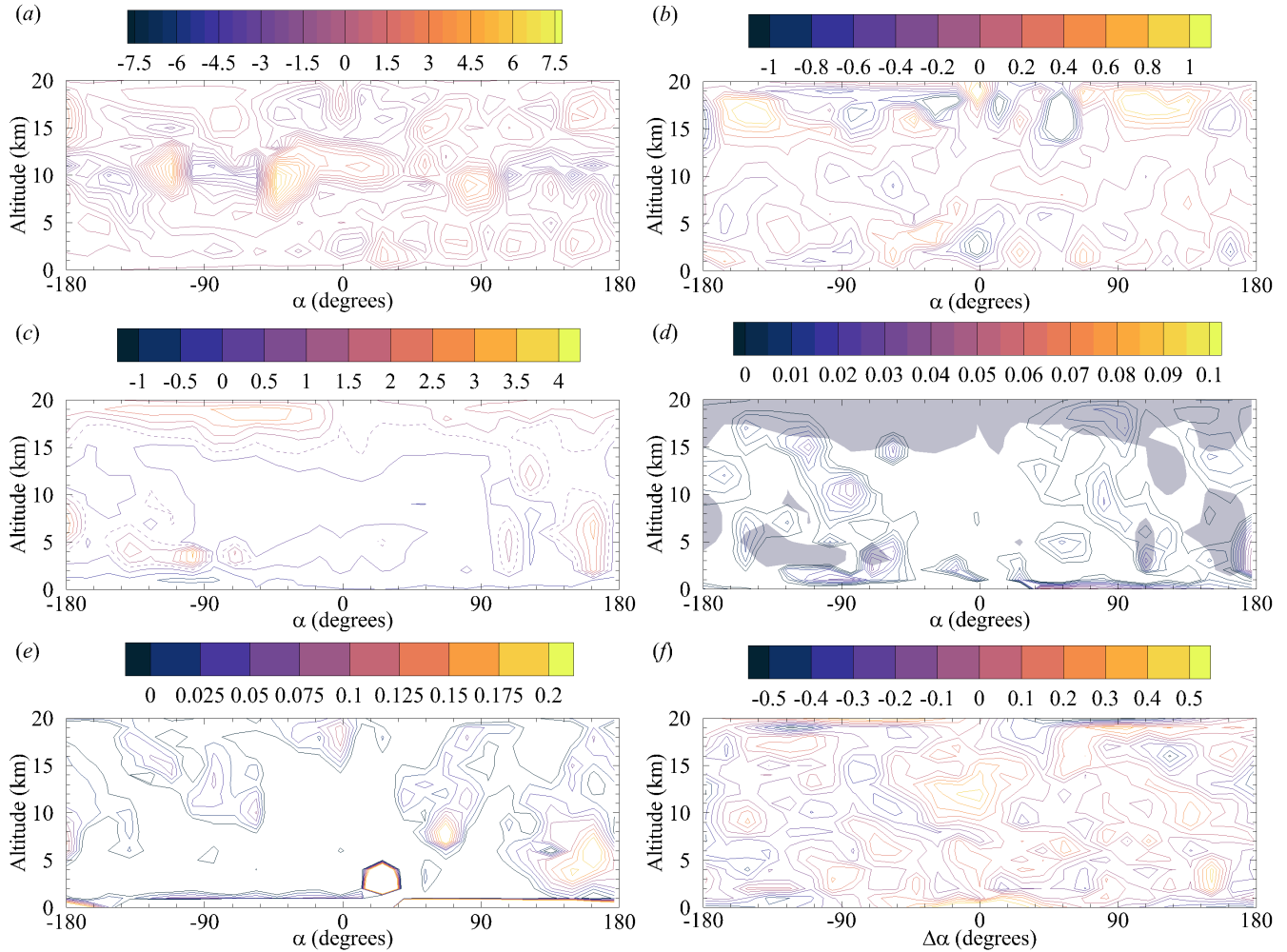
Figure 13. Interpolated values for Flight 2 of: (*a*) $\langle T \rangle'$ in $°C$; (*b*) $\langle w \rangle'$ in m s^{-1}; (*c*) Ri; (*d*) EDR' in m$^{2/3}$ s^{-1}; (*e*) $\left(\log_{10} \sigma_{IS}^2 \right)'$ in $\log_{10}(\text{Pa}^2)$; and (f) $R(\Delta\alpha, z)$, the cross-correlation of EDR' and $\left(\log_{10} \sigma_{IS}^2 \right)'$. Dashed lines in (*c*) and shaded regions in (*d*) identify the boundary where $Ri = 1$.

indicating that the turbulence here is produced via vertical shearing and clarifies the presence of elevated EDR at stable values of Ri shown in Fig. 11a.

Within the troposphere, a large region elevated EDR' was also present in the easternmost portion of the orbit. This region closely corresponds to a region of reduced stability where $Ri < 1$, and therefore can be attributed to turbulence produced by thermally-driven motions. Interestingly, in this visualization, their trajectories can also be identified. For instance, turbulence initiating in the boundary layer near $\alpha = 0°$ can be seen to have traveled eastward with the wind, extending through the tropopause until it reached the more stable stratosphere at $\alpha \approx -170°$ and appears to be connected to the initiation of the
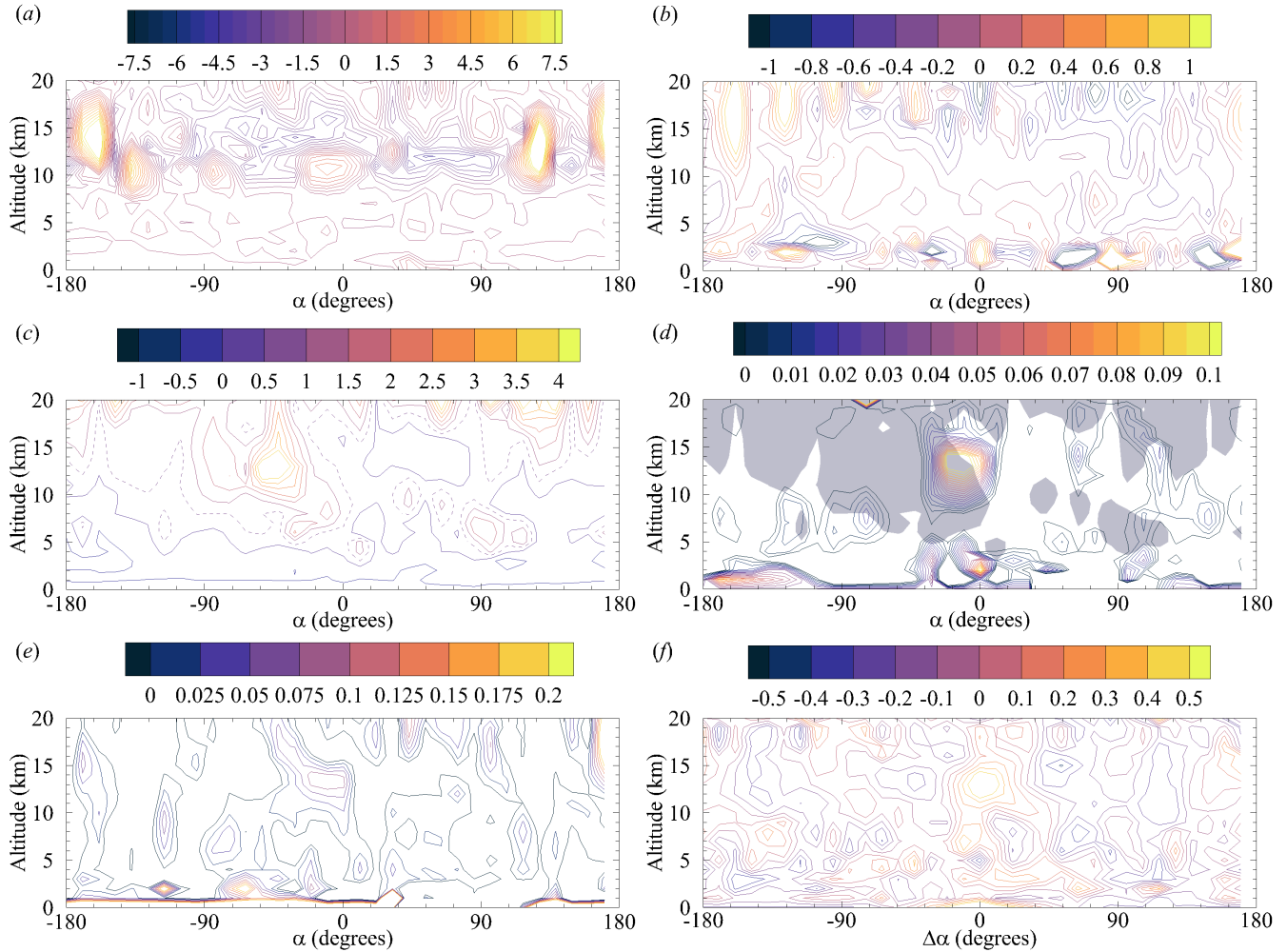
Figure 14. Interpolated values for Flight 3 of: (a) $\langle T \rangle'$ in $^\circ C$; (b) $\langle w \rangle'$ in m s^{-1}; (c) Ri; (d) EDR' in m$^{2/3}$ s^{-1}; (e) $\left(\log_{10}\sigma_{IS}^2\right)'$ in $\log_{10}(\text{Pa}^2)$; and (f) $R(\Delta\alpha, z)$, the cross-correlation of EDR' and $\left(\log_{10}\sigma_{IS}^2\right)'$. Dashed lines in ($c$) and shaded regions in (d) identify the boundary where $Ri = 1$.

gravity waves and enhanced EDR' in the stratosphere, suggesting that the gravity wave observed at the tropopause within this region may have been initiated by the air rising from the boundary layer.

455   Finally, we can also revisit the infrasonic microphone response measured during Flight 1 using these visualizations. When the altitude dependence of the microphone response is removed through the averaging and decomposition process described in equation 11, the areas where elevated response was measured become more clearly related to the atmospheric motions. Note that to better highlight the microphone response, the decomposition was applied to the logarithm of the signal variance, specifically $\log_{10}\sigma_{IS}^2$. The resulting visualization of $(\log_{10}\sigma_{IS}^2)'$ is shown in Fig. 12e. When viewed in this manner, regions of

460   elevated infrasonic signal closely correspond to regions of elevated EDR', although there are structural differences between

the two. The closest correspondence is not surprisingly where EDR' was highest, such as in the boundary layer and in the stratosphere around $80° < \alpha < 130°$. Within the troposphere the region attributed to buoyant rising air was also a region where elevated $(\log_{10}\sigma_{IS}^2)'$ was measured, although over a broader range of α.

To quantify the relationship between $(\log_{10}\sigma_{IS}^2)'$ and EDR' we can use the cross-correlation of the two distributions shown in Fig. 12e and f. This was conducted over each 1 km bin of z shown in Fig. 12 such that

$$R(\Delta\alpha, z) = \frac{\overline{\left(C(z,\alpha) - \overline{C}(\alpha)\right)\left(D(z,\alpha) - \overline{D}(\alpha + \Delta\alpha)\right)}}{\overline{\left(C(z,\alpha) - \overline{C}(\alpha)\right)^2}^{1/2}\overline{\left(D(z,\alpha) - \overline{D}(\alpha)\right)^2}^{1/2}} \tag{12}$$

where $C = EDR'$ and $D = (\log_{10}\sigma_{IS}^2)'$ and the overline once again indicates a bin average at over each 1 km bin of z. Note that, due to the circular nature of the flight trajectory, the quantities C and D are treated as periodic in α, allowing for the cross-correlation to be calculated for $-180° < \Delta\alpha < 180°$. The resulting distribution of $R(\Delta\alpha, z)$ is shown in Fig. 12f. This figure confirms the strong correlation between the two quantities, with peak correlation values of $R > 0.5$ calculated for $\Delta\alpha = 0$. In the z regions where higher EDR' was observed, specifically the boundary layer and stratosphere, the correlation drops off rapidly, suggesting that the strongest infrasonic microphone response was when the aircraft was within the turbulence. However, in the troposphere, where the EDR' values were lower, the microphone response appears to have increased before the aircraft reached the region of elevated EDR' by $\Delta\alpha \approx 90°$, or approximately 2 km. Note, however, that this was the only flight where such a clear shift in $\Delta\alpha$ was as evident (see Figs. 13f and 14f), which may indicate that this result was an outlier, or may reflect the influence of the more complicated atmospheric structure measured during the latter flights.

The organization of structural features measured during Flight 2 are shown in Fig. 13. During this flight, the troposphere and lower stratosphere ($z < 15$ km) were much less stable than they were for Flight 1, as indicated by the Ri distributions shown in Fig. 13c. Measurements of EDR' shown in Fig. 13d indicate that vertical structures of increased turbulence were present, stretching from the boundary layer to the stratosphere, that are consistent with the turbulence production expected due to the vertical shearing by buoyancy-driven motions. These locations of enhanced EDR' coincide with strong perturbations measured at the tropopause ($z \approx 10$ km), suggesting that these perturbations were caused by vertical transport of warmer air. Interestingly, there does not appear to be a strong signature of these motions in the $\langle w \rangle'$ distributions within the tropopause (Fig. 13b). However strong $\langle w \rangle'$ perturbations were observed in the stratosphere ($z > 15$ km), particularly in the range $-45° < \alpha < 90°$ and throughout this layer, which indicate the presence of stratospheric gravity waves during this flight. The gravity wave signature in the range $-45° < \alpha < 90°$ also coincides to the presence of enhanced EDR' and accounts for the high EDR values measured at high Ri in Fig. 11b.

As with Flight 1, the infrasonic signal distributions shown in Fig. 13e closely correspond to the EDR' distributions of Fig. 13d. Strong correlation between these two quantities was also observed, with $R(\Delta\alpha, z)$, particularly near $\delta\alpha = 0$. However the distribution of $R(\Delta\alpha, z)$ is more difficult to interpret, perhaps due to the presence of multiple regions of enhanced EDR' and $(\log_{10}\sigma_{IS}^2)'$ present at the same altitude and the correlation unable to distinguish between individual contributions. This could also be compounded by the different modalities of the sensors, with EDR' being measured by an in-situ sensor whereas

$(\log_{10} \sigma_{IS}^2)'$ was measured by a remote-sensing device. This latter point could further obfuscate the correlations as higher $(\log_{10} \sigma_{IS}^2)'$ may be produced by motions outside the flight path of the in-situ sensor.

495   The visualizations for Flight 3, shown in Fig. 14, reveal similar structural features existed during this flight as with Flights 1 and 2. For example, the $\langle T \rangle'$ distribution in Fig. 14a shows strong periodic perturbations in temperature extended from the tropopause to the stratosphere (10 km$< z <$20 km) for $\alpha > 100°$ and $\alpha < 130°$. When compared to the $\langle w \rangle'$ distributions, it appears that these perturbations may have arose from a single gravity wave initiating in the boundary layer near $\alpha = 45°$ and ascending in the positive α direction and reaching $z \approx 20$ km at $\alpha \approx -80°$. The corresponding Ri distribution in Fig 14c indi-

500 cates that a horizontal mixture of stable and unstable conditions existed which, when viewed via the thresholding at $Ri = 1$ as done in Fig. 14d bears striking similarity to the structure produced by a tropopause fold. Also consistent with the characteristics of a tropopause fold is the presence of enhanced EDR' along the $Ri = 1$ boundary, created by vertical shearing motions, with an intense region of turbulence near $\alpha = 0°$ and $z = 12$ km. The overlap of these enhanced EDR' regions into the $Ri > 1$ regions again clarifies the presence of high EDR at high Ri shown in Fig. 11c. Also evident in Fig. 14d is that increased

505 EDR' was measured for $z < 10$ km in the range $-180° < \alpha < -45°$ that is consistent with the vertical mixing associated with a thermal plume forming in the presence of unstable conditions (Fig. 14c) within this portion of the flight path.

For this flight the infrasonic microphone response, as reflected in the $(\log_{10} \sigma_{IS}^2)'$ distribution, was less easily related to the EDR' distribution than for Flights 1 or 2. Similar features can be observed in the EDR' and $(\log_{10} \sigma_{IS}^2)'$ distributions at similar locations, but the $(\log_{10} \sigma_{IS}^2)'$ distribution contains numerous additional regions where increased infrasonic amplitude

510 was measured with no commensurate region of enhanced EDR'. As with Flight 2, this results in a $R(\Delta \alpha, z)$ correlation pattern that is difficult to provide an interpretation. However, horizontal periodicity with a period of $\Delta \alpha \approx 90°$ is evident in the $R(\Delta \alpha, z)$ distributions in the range 5 km$< z <$15 km. This horizontal periodicity could indicate that the same turbulent sound-generating events are being picked up by the infrasonic microphone at different portions of the flight profile.

4   Summary and Conclusions

515 This work demonstrates how a sUAS in the form of a balloon-launched glider can be used to conduct detailed analysis of the statistical structure of atmospheric turbulence over a range of altitudes typically interrogated using weather balloons. In the measurements described here, the particular aircraft was equipped with a five-hole-probe for measuring the three-component wind vector, and a pressure, temperature and humidity sensing system integrated into the aircraft.

These instruments allowed the calculation of vertical profiles of T, RH, U and dir which compared favorably with publicly-

520 available radiosonde data from a site located 160 km away. In addition, the slow, spiralling descent allowed for the calculation of time-averaged statistics such as k and ε with high vertical resolution. The resulting vertical profiles suggest that isolated regions of of turbulence were present in all three flights, although enhanced values of ε in the stratosphere, represented using EDR, were produced despite the kinetic energy content not containing the characteristic roll-off expected for inertial range turbulence. Furthermore, a comparison of the flux Richardson number and and the EDR measured at the same location

525 suggested that there was only a general connection between the two parameters, with multiple measurements of turbulent values of EDR made in regions identified as being stable through the corresponding values of Ri measured at those locations.

However, by taking advantage of the horizontal trajectory taken by the glider during its descent, it was also possible to produce depictions of multiple parameters measured during the descent. When the altitude-dependent trends were removed from the parameters, it became possible to visualize the structure of the motions measured along the flight path. These visualizations
530 were found to show that many of the features which appear in isolation on the vertical profiles were actually produced by vertically aligned structures. Using these visualizations also revealed that the increased k and EDR in the stratosphere corresponded to the presence of gravity waves and momentum transfer associated with coupling between two layers of different waves. Other gravity waves were found to initiate from the boundary layer and transport up to the stratosphere, in some cases appearing to initiate the measured wave structure. Although the source of these waves could not be definitively identified, one
535 likely source is that of mountain waves, due to the topography around the flight area which consisted of 1 km high mountain ranges to the east and west. In support of this hypothesis is the observation that for the two flights where the most wave activity was observed, the winds were coming from the west and northwest, which would result in the flight path being in the lee of the western mountain range. The second flight, for which fewer wave signatures were measured, had winds more directly from the north.

540 These measurements also allowed the identification of the presence of large thermals, as well as evidence of the presence of a tropopause fold. These features were associated with the presence of local regions of increased turbulence and thus the sUAS measurements enabled the connection between regions of increased turbulence and their generating mechanisms and it would be difficult to draw the same associations using balloon-based measurements. This ability is directly related to the aircraft's measurement profile as the platform provides a high resolution interrogation of the atmospheric properties over a large vertical
545 and horizontal extent. From a purely statistical viewpoint, the ability of the aircraft to orbit around a fixed geographical point, rather than travelling with the wind, eases interpretation of the measurements. In addition the flight pattern allows for increased statistical convergence due to the longer time the aircraft spends at a particular altitude range.

Finally, a secondary objective of this study was to assess the feasibility of implementing an infrasonic microphone on a sUAS for detecting clear air turbulence. The results of this study indicate that the infrasonic microphone can detect turbulent
550 features, with similar structural organization measured in the microphone response to that measured by the five-hole-probe. However, the remote sensing nature of this instrument, its altitude sensitivity, and the broad-band nature of turbulent sound generation make it challenging to discriminate discrete turbulent events from a single microphone.

Data availability. Data from these flights are available from the corresponding author on request.

Video supplement. A video compilation of aircraft preparation, flight and recovery is publicly available at https://vimeo.com/568101900

References

Abarbanel, H. D. I., Holm, D. D., Marsden, J. E., and Ratiu, T.: Richardson Number Criterion for the Nonlinear Stability of Three-Dimensional Stratified Flow, Phys. Rev. Lett., 52, 2352–2355, https://doi.org/10.1103/PhysRevLett.52.2352, 1984.

565 Al-Ghussain, L. and Bailey, S. C. C.: Uncrewed Aircraft System Measurements of Atmospheric Surface-Layer Structure During Morning Transition, Boundary-Layer Meteorology, 185, 229–258, https://doi.org/10.1007/s10546-022-00729-2, 2022.

Bailey, S. C. C., Canter, C. A., Sama, M. P., Houston, A. L., and Smith, S. W.: Unmanned aerial vehicles reveal the impact of a total solar eclipse on the atmospheric surface layer, Proceedings of the Royal Society A: Mathematical, Physical and Engineering Sciences, 475, 20190 212, https://doi.org/10.1098/rspa.2019.0212, 2019.

570 Balsley, B. B., Lawrence, D. A., Woodman, R. F., and Fritts, D. C.: Fine-scale characteristics of temperature, wind, and turbulence in the lower atmosphere (0–1,300 m) over the south Peruvian coast, Boundary-Layer Meteorology, 147, 165–178, 2013.

Bärfuss, K., Pätzold, F., Altstädter, B., Kathe, E., Nowak, S., Bretschneider, L., Bestmann, U., and Lampert, A.: New setup of the UAS ALADINA for measuring boundary layer properties, atmospheric particles and solar radiation, Atmosphere, 9, https://doi.org/10.3390/atmos9010028, 2018.

575 Bohn, D. and Simon, H.: Mehrparametrige Approximation der Eichräume und Eichflächen von Unterschall-bzw. Überschall-5-Loch-Sonden, tm-Technisches Messen, 468, 81–89, 1975.

Bowman, D. C. and Lees, J. M.: Infrasound in the middle stratosphere measured with a free-flying acoustic array, Geophysical Research Letters, 42, https://doi.org/10.1002/2015GL066570, 2015.

Chunchuzov, I. P., Kulichkov, S. N., Popov, O. E., and Perepelkin, V. G.: Infrasound generation by meteorological fronts and its propagation
580 in the atmosphere, https://doi.org/10.1175/jas-d-20-0253.1, 2021.

Cuxart, J., Tatrai, D., Weidinger, T., Kircsi, A., Józsa, J., and Kiss, M.: Infrasound as a Detector of Local and Remote Turbulence, Boundary-Layer Meteorology, 159, 185–192, https://doi.org/10.1007/s10546-015-0100-2, 2015.

Egger, J., Bajrachaya, S., Heingrich, R., Kolb, P., Lammlein, S., Mech, M., Reuder, J., Schäper, W., Shakya, P., Shween, J., and H., W.: Diurnal Winds in the Himalayan Kali Gandaki Valley. Part III: Remotely Piloted Aircraft Soundings, Mon. Wea. Rev., 130, 2042–2058,
585 2002.

Ehrenberger, L. J.: Stratospheric Turbulence Measurements and Models for Aerospace Plane Design, Tech. Rep. TM-104262, NASA, 1992.

Enlich, R. and Mancuso, R.: The Turbulence Climatology of the United States between 20,000 and 45,000 Feet Estimated from Aircraft Reports and Meteorological Data, Tech. rep., Stanford Research Institute, https://apps.dtic.mil/sti/pdfs/AD0672988.pdf, 1968.

Fujiwara, M., Yamamoto, M. K., Hashiguchi, H., Horinouchi, T., and Fukao, S.: Turbulence at the tropopause due to breaking Kelvin waves
590 observed by the Equatorial Atmosphere Radar, Geophysical Research Letters, 30, https://doi.org/https://doi.org/10.1029/2002GL016278, 2003.

Galperin, B., Sukoriansky, S., and Anderson, P. S.: On the critical Richardson number in stably stratified turbulence, Atmospheric Science Letters, 8, 65–69, https://doi.org/https://doi.org/10.1002/asl.153, 2007.

Haack, A., Gerding, M., and Lübken, F.-J.: Characteristics of stratospheric turbulent layers measured by LITOS and their relation to the
595 Richardson number, Journal of Geophysical Research: Atmospheres, 119, 10,605–10,618, https://doi.org/10.1002/2013JD021008, 2014.

Hamilton, J., de Boer, G., Doddi, A., and Lawrence, D. A.: The DataHawk2 uncrewed aircraft system for atmospheric research, Atmospheric Measurement Techniques, 15, 6789–6806, https://doi.org/10.5194/amt-15-6789-2022, 2022.

Hobbs, S., Dyer, D., Courault, D., Olioso, A., Lagouarde, J.-P., Kerr, Y., McAnneney, J., and Bonnefond, J.: Surface layer profiles of air temperature and humidity measured from unmanned aircraft, Agronomie, 22, 635–640, https://doi.org/10.1051/agro:2002050, 2002.

600 Huang, R., Sun, H., Wu, C., Wang, C., and Lu, B.: Estimating Eddy Dissipation Rate with QAR Flight Big Data, Applied Sciences, 9, 5192, https://doi.org/10.3390/app9235192, 2019.

Jacob, J. D., Chilson, P. B., Houston, A. L., and Smith, S. W.: Considerations for Atmospheric Measurements with Small Unmanned Aircraft Systems, Atmosphere, 9, https://doi.org/10.3390/atmos9070252, 2018.

Kim, S.-H., Chun, H.-Y., Kim, J.-H., Sharman, R. D., and Strahan, M.: Retrieval of eddy dissipation rate from derived equivalent

605 vertical gust included in Aircraft Meteorological Data Relay (AMDAR), Atmospheric Measurement Techniques, 13, 1373–1385, https://doi.org/10.5194/amt-13-1373-2020, 2020.

Kolmogorov, A. N.: The local structure of turbulence in incompressible viscous fluid for very large Reynolds numbers, Dokl. Akad. Nauk SSSR, 30, 301–305, 1941.

Lenschow, D.: The measurement of air velocity and temperature using the NCAR Buffalo aircraft measuring system, National Center for

610 Atmospheric Research, 1972.

Pope, S. B.: Turbulent Flows, Cambridge University Press, 2000.

Rautenberg, A., Graf, M. S., Wildmann, N., Platis, A., and Bange, J.: Reviewing wind measurement approaches for fixed-wing unmanned aircraft, Atmosphere, 9, 1–24, https://doi.org/10.3390/atmos9110422, 2018.

Shams, Q. A., Zuckerwar, A. J., Burkett, C. G., Weistroffer, G. R., and Hugo, D. R.: Experimental investigation into infrasonic emissions

615 from atmospheric turbulence, The Journal of the Acoustical Society of America, 133, 1269–1280, https://doi.org/10.1121/1.4776180, 2013.

Shapiro, M. A.: Turbulent Mixing within Tropopause Folds as a Mechanism for the Exchange of Chemical Constituents between the Stratosphere and Troposphere, Journal of Atmospheric Sciences, 37, 994 – 1004, https://doi.org/10.1175/1520-0469(1980)037<0994:TMWTFA>2.0.CO;2, 1980.

620 Sharman, R. D., Cornman, L. B., Meymaris, G., Pearson, J., and Farrar, T.: Description and Derived Climatologies of Automated In Situ Eddy-Dissipation-Rate Reports of Atmospheric Turbulence, Journal of Applied Meteorology and Climatology, 53, 1416–1432, https://doi.org/10.1175/JAMC-D-13-0329.1, 2014.

Söder, J., Zülicke, C., Gerding, M., and Lübken, F.-J.: High-Resolution Observations of Turbulence Distributions Across Tropopause Folds, Journal of Geophysical Research: Atmospheres, 126, https://doi.org/10.1029/2020JD033857, 2021.

625 Treaster, A. L. and Yocum, A. M.: The calibration and application of five-hole probes, Tech. rep., DTIC Document, 1978.

van den Kroonenberg, A., Martin, T., Buschmann, M., Bange, J., and Vörsmann, P.: Measuring the Wind Vector Using the Autonomous Mini Aerial Vehicle M^{2}AV, J. Atmos. Oceanic Technol., 25, 1969–1982, 2008.

Wescott, J., SCIENCE, M. U. A. A. I. O., and TECHNOLOGY.: Acoustic Detection of High - Altitude Turbulence, Defense Technical Information Center, https://books.google.com/books?id=pkBFGwAACAAJ, 1964.

630 Whitaker, R. W. and Norris, D. E.: Infrasound Propagation, https://doi.org/10.1007/978-0-387-30441-0_82, 2008.

Wildmann, N., Hofsäß, M., Weimer, F., Joos, A., and Bange, J.: MASC–a small Remotely Piloted Aircraft (RPA) for wind energy research, Advances in Science and Research, 11, 55–61, 2014.

Witte, B. M., Singler, R. F., and Bailey, S. C.: Development of an Unmanned Aerial Vehicle for the Measurement of Turbulence in the Atmospheric Boundary Layer, Atmosphere, 8, 195, 2017.